1 **PI(4,5)P$_2$ forms dynamic cortical structures and directs actin**
2 **distribution and cell polarity in *C. elegans* embryos**
3

4 Melina J. Scholze[(1)], Kévin S. Barbieux[(2)], Alessandro De Simone[(1,3)], Mathilde
5 Boumasmoud[(1,4)], Camille C. N. Süess[(1)], Ruijia Wang[(1)], and Pierre Gönczy[(1)]

6 (1) Swiss Institute for Experimental Cancer Research (ISREC), School of Life Sciences, Swiss
7   Federal Institute of Technology (EPFL), Lausanne, Switzerland
8 (2) Geodetic Engineering Laboratory (TOPO), Swiss Federal Institute of Technology (EPFL),
9   Environmental Engineering Institute (IIE), Lausanne Switzerland

10

11 Present addresses:

12 (3) Department of Cell Biology, Duke University Medical Center, Durham 27710 USA
13 (4) Division of Infectious Diseases and Hospital Epidemiology, University Hospital Zürich,
14   University of Zürich, Zürich, Switzerland

15

16 Corresponding author: Pierre Gönczy (pierre.gonczy@epfl.ch)

17 3-6 key words: *C. elegans* embryo, Phosphoinositiodes, PIP$_2$, asymmetric cell
18 division, actin, PAR polarity.

19 Summary statement: PI(4,5)P$_2$ is distributed in dynamic cortical structures and
20 regulates asymmetric division by controlling actin organization and cell polarity in the
21 one-cell *C. elegans* embryo.

Abstract

Asymmetric division is crucial for embryonic development and stem cell lineages. In the one-cell *C. elegans* embryo, a contractile cortical actomyosin network contributes to anterior-posterior (A-P) polarity and asymmetric division by segregating PAR proteins to discrete cortical domains. Here, we discovered that the plasma membrane lipid phosphatidylinositol 4,5-bisphosphate (PIP$_2$) forms dynamic structures in *C. elegans* zygotes, distributing in a polarized and PAR-dependent manner along the A-P axis. PIP$_2$ cortical structures overlap with F-actin and coincide with the actin regulators RHO-1, CDC-42 and ECT-2. Particle image velocimetry analysis revealed that PIP$_2$ and F-actin cortical movements are coupled, with PIP$_2$ structures moving slightly ahead. Importantly, we established that PIP$_2$ cortical structures form in an actin-dependent manner and, conversely, that decreasing or increasing the level of PIP$_2$ results in severe F-actin disorganization, revealing the interdependence between these components. Furthermore, we uncovered that PIP$_2$ regulates the sizing of PAR cortical domains. Overall, our work establishes for the first time that a lipid membrane component, PIP$_2$, is a critical modulator of actin organization and cell polarity in *C. elegans* embryos.

Introduction

43

44 Asymmetric division generates cellular diversity and is particularly prevalent during

45 development. During intrinsic asymmetric division, polarity is established and

46 maintained in a mother cell; thereafter, polarity is translated into correct spindle

47 positioning during mitosis along this polarity axis, resulting in the proper cleavage

48 and partition of cellular contents to daughter cells. The extensively studied and

49 evolutionarily conserved partitioning defective (PAR) proteins are critical for cell

50 polarity and asymmetric division (reviewed in Goldstein and Macara, 2007; Gönczy,

51 2008; Knoblich, 2010). By contrast to the wealth of knowledge regarding PAR

52 proteins and interacting components, the involvement of lipid plasma membrane

53 components in cell polarity is less understood, in particular in developing systems.

54 The early *C. elegans* embryo has proven instrumental for dissecting the

55 mechanisms governing asymmetric division (reviewed in Hoege and Hyman, 2013;

56 Pacquelet, 2017; Rose and Gönczy, 2014). Shortly after fertilization, the entire

57 embryo surface exhibits uniform contractions of the cortical actomyosin network

58 located underneath the plasma membrane (Munro et al., 2004). These contractions

59 are driven by non-muscle myosin 2 (NMY-2), which is activated by the Rho GTPase

60 RHO-1 and its guanine nucleotide exchange factor (GEF) ECT-2 (Motegi and

61 Sugimoto, 2006; Schonegg and Hyman, 2006). Sperm-derived centrioles are key for

62 breaking symmetry of this system and for inducing local disappearance of cortical

63 ECT-2 in their vicinity, thereby determining the embryo posterior. This leads to local

64 inactivation of RHO-1 and initiation of cortical flows away from this region, towards

65 the future embryo anterior (Bienkowska and Cowan, 2012; Cowan and Hyman, 2004;

66 Motegi and Sugimoto, 2006). Polarized contractility promotes establishment of PAR

67 polarity, whereby PAR-3, PAR-6, and atypical protein kinase C-like 3 (PCK-3) are

68 segregated to the anterior side, whereas PAR-1, PAR-2, and Larval Giant Larvae-like

69 1(LGL-1) occupy the expanding posterior cortical domain (reviewed in Hoege and

70 Hyman, 2013; Pacquelet, 2017; Rose and Gönczy, 2014). The RhoGTPase CDC-42

71 is also segregated to the anterior, where it stabilizes the actomyosin network and

72 promotes PAR-6 association with the cortex (Kumfer et al., 2010; Motegi and

73 Sugimoto, 2006; Schonegg and Hyman, 2006).

74 PAR polarity can be established in *C. elegans* zygotes also though a partially

75 redundant pathway, whereby microtubules nucleated from centrosomes protect PAR-

76   2 from PKC-3-mediated phosphorylation, thus allowing PAR-2 association with

77   phospholipids at the embryo posterior (Motegi et al., 2011). In other systems,

78   homologues of PAR proteins and interacting components also associate with

79   phospholipids, as exemplified by *Drosophila* DmPar3 binding to phosphatidylinositol

80   4,5-bisphosphate (PI(4,5)P_2, referred to hereafter as PIP_2 for simplicity) and

81   phosphatidylinositol 3, 4,5-triphosphate (PI(4,5,6)P_3, hereafter PIP_3) (Krahn et al.,

82   2010). Furthermore, human Cdc42 binds to PIP_2 (Johnson et al., 2012). Overall,

83   whereas it is clear that phospholipids can bind PARs and interacting proteins in some

84   contexts, their subcellular distribution and potential function in an asymmetrically

85   dividing system such as the *C. elegans* zygote remain unclear.

86   PIP_2 is the most abundant of seven phosphorylated phosphatidylinositols and

87   is present mostly in the inner leaflet of the plasma membrane, as revealed for

88   instance by the distribution of the pleckstrin homology (PH) domain of mammalian

89   phospholipase C1δ1 (PLC1 δ1), which binds PIP_2 *in vitro* and in cells with high

90   specificity (Garcia et al., 1995; Lemmon et al., 1995; Várnai and Balla, 1998). PIP_2 is

91   mainly phosphorylated from phosphatidylinositol 4-phosphate PI(4)P (PIP) by Type I

92   PI(4)P5-kinases (PIP5K1), and can be further phosphorylated to PIP_3 by

93   Phosphatidylinositol 3-kinases (PI3K). Conversely, PIP_2 can be dephosphorylated by

94   5-phosphatases, including OCRL and synaptojanin (reviewed in Brown, 2015; De

95   Craene et al., 2017; McLaughlin et al., 2002). Amongst other roles, in systems from

96   *S. cerevisiae* to *H. sapiens,* PIP_2 helps link the F-actin cortical network to the plasma

97   membrane, as well as stimulate F-actin assembly and reorganization. The latter

98   function is achieved notably by activating, together with Cdc42, WASP family

99   proteins that, in turn, activate the actin nucleator Arp2/3. Moreover, PIP_3 further

100   activates WASP family proteins through RhoGTPase GEFs (reviewed in Brown,

101   2015; De Craene et al., 2017; Di Paolo and De Camilli, 2006; McLaughlin et al.,

102   2002; Wu et al., 2014; Yin and Janmey, 2003; Zhang et al., 2012). Whether and, if

103   so, how, PIP_2 regulates cortical actomyosin network organization in the *C. elegans*

104   embryo is not known.

105   Not only is the potential function of PIP_2 in the *C. elegans* zygote not clear, but

106   the same holds for PIP_2 subcellular distribution. In other systems, PIP_2 can distribute

107   unevenly in the plasma membrane, for instance accumulating in macrodomains in

108   nascent phagosomes, in membrane ruffles or at the leading edge of motile cells,

109 which all exhibit curved membranes that are sites of actin reorganization (Chierico et

110 al., 2015; McLaughlin et al., 2002; Zhang et al., 2012). Accordingly, PIP_2 can

111 stimulate actin polymerization in curved but not flat model membranes (Gallop et al.,

112 2013). Interestingly, PIP_2 patches assemble at the leading edge of neuronal PC12

113 cells prior to F-actin patch accumulation, but their formation also depends on F-actin

114 (Golub and Caroni, 2005; Golub and Pico, 2005). Moreover, it was suggested that F-

115 actin enrichment in cell cortices drives clustering of PIP_2-containing macrodomains,

116 which in turn further regulate actin polymerization and branching (reviewed in Chichili

117 and Rodgers, 2009). Overall, PIP_2 and F-actin polymerization function in a positive

118 feedback mechanism in several systems.

119   The single PIP5K1 in *C. elegans* is PPK-1, which can synthesize PIP_2 from

120 PIP *in vitro* and *in vivo* (Weinkove et al., 2008). Overexpression of PPK-1 in

121 developing worm neurons increases the level of PIP_2 and results in extended

122 filopodial-like structures, probably through changes in the actin cytoskeleton

123 (Weinkove et al., 2008). In the somatic gonad, PPK-1 is important for F-actin

124 cytoskeletal reorganization and, therefore, gonad contractility (Xu et al., 2007).

125 Moreover, PPK-1 is enriched on the posterior cortex of one-cell embryos and has

126 been reported to be important for asymmetric spindle positioning, but not for cell

127 polarity (Panbianco et al., 2008). In other systems, however, PIP_2 can regulate cell

128 polarity through its ability to recruit PAR proteins and reorganize the actin

129 cytoskeleton. Thus, in the *Drosophila* follicular epithelium, PIP_2 recruits DmPar3 to

130 the apical plasma membrane to maintain apical-basal polarity (Claret et al., 2014).

131 Moreover, PIP_2 might mediate interactions between PAR proteins, the actomyosin

132 network and the plasma membrane in the fly oocyte (Gervais et al., 2008), as well as

133 regulate apical constriction in the fly embryo (Guglielmi et al., 2015). Motile cells such

134 as mammalian neurophils or *Dictyostelium discoideum* also rely on PIP_2, together

135 with PIP_3, for actin network reorganization and polarization (reviewed in Wu et al.,

136 2014). To summarize, in many systems, PIP_2 is essential for F-actin reorganization

137 and cell polarization, but it remains to be investigated whether this is the case in the

138 developing *C. elegans* embryo.

Results

The PIP$_2$ biomarker GFP::PH$^{PLC1\delta1}$ is present in dynamic polarized cortical structures in one-cell *C. elegans* embryos

While monitoring the distribution of components involved in asymmetric division of the *C. elegans* zygote with confocal spinning disk microscopy, we found that the PIP$_2$ biomarker GFP::PH$^{PLC1\delta1}$ (Audhya et al., 2005) forms distinct and dynamic structures at the cell cortex (Fig. 1A-J; Fig. S1A; Movie 1). Initially, when the cortical actomyosin network is contractile throughout the embryo, PIP$_2$ is present weakly and evenly on the cell cortex (data not shown). Thereafter, when the actomyosin network begins to retract towards the anterior at the onset of polarity establishment, we observed the appearance of striking elongated cortical structures enriched in PIP$_2$, primarily on the anterior side of the embryo (Fig. 1A, B, 1K; Fig. S1A, top). Such PIP$_2$ cortical structures have an average size of ~2.5 µm^2 and further elongate over time as the cell progresses through the cell cycle (Fig. 1L, M). Subsequently, all elongated PIP$_2$ cortical structures move anteriorly so that they become distributed in a clearly polarized manner at pseudocleavage, which marks the end of the polarity establishment phase (Fig. 1C, D, arrow). At this time, PIP$_2$ structures cover ~15% of the anterior cortical surface (Fig. 1K). During the centration/rotation stage that follows, PIP$_2$ cortical structures first decrease in size (Fig. 1E, F, arrowhead), with most of them disappearing completely but some remaining as small foci by the time the cell enters mitosis (Fig. 1G, H, arrowheads). A few elongated cortical structures reappear during cytokinesis, primarily in the embryo anterior (Fig. 1I, J). In contrast to the discrete structures visible when imaging the cortical plane, PIP$_2$ entities are barely detectable in the embryo middle plane (Fig. S1A, bottom), likely explaining why they were not reported previously (Audhya et al., 2005; Blanchoud et al., 2010; Panbianco et al., 2008).

We set out to verify the cortical distribution revealed by GFP::PH$^{PLC1\delta1}$ using fluorescently labeled synthetic PIP$_2$. To this end, we delivered Bodipy-FL-PIP$_2$ lipids to embryos whose eggshell had been permeabilized using *perm-1*(*RNAi*) (Carvalho et al., 2011). Although there was a high background of fluorescent lipids outside the embryo, we found that Bodipy-FL-PIP$_2$ distributes in cortical structures marked by mCherry::PH$^{PLC1\delta1}$ (Fig. S1B, C). Overall, we conclude that PIP$_2$ forms dynamic and polarized structures at the plasma membrane of one-cell *C. elegans* embryos.

6

A-P polarity cues regulate the polarized distribution of PIP_2 cortical structures

173 We set out to address what regulates the polarized distribution of PIP_2 cortical

174 structures, which is particularly apparent during the pseudocleavage stage, as

175 evidenced also by the fact that they do not overlap with GFP::PAR-2, which marks

176 the posterior cortical domain (Fig. 2A). By contrast, we found that PIP_2 cortical

177 structures overlap with the anterior polarity domain harboring GFP::PAR-6 (Fig. 2B;

178 Movie 2). Moreover, we observed that PIP_2 cortical structures overlap only with

179 elongated GFP::PAR-6 cortical structures (Fig. 2B, arrow), but not with GFP::PAR-6

180 foci (Fig. 2B, arrowhead), which are two distinct cortical populations of GFP::PAR-6

181 previously reported to exist (Beers and Kemphues, 2006; Robin et al., 2014;

182 Rodriguez et al., 2017; Wang et al., 2017).

183   We next tested whether the polarized distribution of PIP_2 cortical structures

184 depends on A-P polarity cues. In contrast to the polarized distribution observed in the

185 control condition, we found that upon *par-3*(*RNAi*), PIP_2 cortical structures distribute

186 essentially uniformly over the cell cortex (compare Fig. 2C, D with 2E, F), except for

187 the very posterior of the embryo, consistent with the known slight posterior clearing of

188 the actomyosin network upon PAR-3 inactivation (Kirby et al., 1990; Munro et al.,

189 2004). Furthermore, we found that upon *par-2(RNAi)*, PIP_2 cortical structures first

190 move anteriorly (Fig. 2G, H), but then become distributed in a more uniform manner

191 (Fig. 2H), in line with PAR-2 being dispensable for polarity establishment, but

192 essential for polarity maintenance (Cuenca et al., 2003; Hao et al., 2006; Munro et

193 al., 2004). Together, these findings establish that the asymmetric distribution of PIP_2

194 cortical structures is regulated by PAR-dependent A-P polarity cues.

195

PIP_2 cortical structures colocalize partially with actin and fully with ECT-2,

RHO-1 and CDC-42

198 Since PIP_2 and F-actin are interdependent in many systems, we tested whether

199 these two components overlap at the cell cortex of *C. elegans* embryos. As shown in

200 Figure 3A and Movie 3, we found a partial overlap of Lifeact::mKate-2, which

201 monitors F-actin, and of PIP_2 cortical structures marked by mNeonGreen::$PH^{PLC1\delta1}$

202 (mNG::$PH^{PLC1\delta1}$). By contrast, we detected no substantial overlap between

203 mCherry::$PH^{PLC1\delta1}$ and GFP::NMY-2 (Fig. 3B; Movie 4), the non-muscle myosin that

204   powers contractions of the cortical actomyosin network (Guo and Kemphues, 1996;

205   Munro et al., 2004). Strikingly, in addition, we found that PIP_2 cortical structures

206   marked by mCherry::PH$^{PLC1\delta1}$ fully colocalize with GFP::ECT-2, GFP::RHO-1 and

207   GFP::CDC-42 (Fig. 2C-E; Movie 5). Overall, we conclude that PIP_2 cortical structures

208   colocalize partially with F-actin, as well as completely with the actomyosin network

209   regulators ECT-2, RHO-1 and CDC-42 in the one-cell *C. elegans* embryo.

210

211   **PIP_2 cortical structures and the F-actin cytoskeleton move in concert**

212   Live imaging of embryos expressing both Lifeact::mKate-2 and mNG::PH$^{PLC1\delta1}$

213   suggested that movements of PIP_2 cortical structures and of the F-actin network are

214   somehow coupled, as drastic changes in PIP_2 cortical structures coincide with

215   alterations in the actomyosin network across the first cell cycle (Movie 3). To

216   investigate this potential coupling in a quantitative manner, we used particle image

217   velocimetry (PIV) to analyze cortical flows of Lifeact::mKate-2 and mNG::PH$^{PLC1\delta1}$ in

218   the same embryo during polarity establishment (Fig. 4A-C) (Thielicke and Stamhuis,

219   2014). This analysis revealed highly correlated local flow velocities at each time point

220   (Fig. 4B; Fig. S2A; Pearson coefficient $\rho = 0.61$, $p<0.0001$). Moreover, the direction

221   of flow vectors at each time point is very similar (Fig. 4C; Fig. S2B; $\theta_{cut\ off}=38°$

222   $p<0.0001$, Material and Methods). Analogous findings were made when comparing

223   mCherry::PH$^{PLC1\delta1}$ and GFP::CDC-42 (Fig. S2C). By contrast, no strong correlation

224   was found between mCherry::PH$^{PLC1\delta1}$ and the caveolin marker CAV-1::GFP (Fig.

225   S2C), which has been suggested to mark lipid rafts in *C. elegans* (Entchev and

226   Kurzchalia, 2005; Kurzchalia and Ward, 2003; Kurzchalia et al., 1999; Merris et al.,

227   2003). Together, these results demonstrate that cortical movements of PIP_2 cortical

228   structures and the F-actin network are coupled.

229   We next addressed whether the movements of PIP_2 cortical structures and of

230   F-actin are synchronous or instead exhibit a time shift that might suggest a potential

231   hierarchy between them, with one component leading the other. Close examination

232   of movies of embryos expressing Lifeact::mKate-2 and mNG::PH$^{PLC1\delta1}$ suggested

233   that PIP_2 cortical structures move slightly ahead of cortical F-actin (Fig. 4E; Movie 6).

234   To address this possibility quantitatively, we cross-correlated time-shifted images of

235   Lifeact::mKate-2 and of mNG::PH$^{PLC1\delta1}$ to determine when there is maximal overlap

236   between the two signals. As shown in Figure 4D, this analysis revealed that maximal

8

237 correlation is achieved when mNeGr::PH$^{PLC1\delta1}$ is on average ~9.3 +/-1.5 seconds

238 ahead of Lifeact::mKate-2. Overall, we conclude that PIP$_2$ cortical structures move

239 together with, but slightly ahead of, F-actin filaments.

240   What drives these movements of PIP$_2$ cortical structures? The observation

241 that PIP$_2$ cortical structures move slightly ahead of F-actin filaments, with the trailing

242 end of PIP$_2$ cortical structure being seemingly in contact with the leading tip of

243 coupled actin filaments (see Fig. 4E), led us to hypothesize that actin polymerization

244 might push PIP$_2$ cortical structures. Compatible with this possibility, we found that the

245 average velocity of PIP$_2$ cortical structures was ~0.17 +/-0.03 μm/s (Fig. S2D, E), in

246 the range of actin polymerization driven motility in other systems (Brangbour et al.,

247 2011; Cameron et al., 2000; Carlsson, 2003; Carlsson, 2010; Mogilner and Oster,

248 1996). These findings lead us to propose that the movements of PIP$_2$ cortical

249 structures are driven by actin polymerization.

250

251 **PIP$_2$ cortical structures depend on F-actin**

252 Given notably the tight coupling between cortical PIP$_2$ structures and F-actin, we

253 investigated whether components of the actomyosin network regulate the presence

254 of PIP$_2$ entities. As shown in Figure 4F, we found that PIP$_2$ cortical structures form

255 and move unabated in *nmy-2*(*RNAi*) embryos, in which actomyosin network

256 contractility is abolished, although they distribute symmetrically, as expected from the

257 known requirement of NMY-2 in A-P polarity (Fig. 4F, G). Therefore, formation and

258 movement of PIP$_2$ cortical structures do not depend on a contractile actomyosin

259 cortex. In stark contrast, we found that PIP$_2$ cortical structures hardly form in *act-*

260 *1*(*RNAi*) embryos (Fig. 4G, H, I; Fig. S3A-D). Moreover, acute impairment of F-actin

261 through treatment of *perm-1*(*RNAi*) embryos with the actin polymerization inhibitor

262 Cytochalasin D led to the disappearance of PIP$_2$ cortical structures (Fig. S3E, F). By

263 contrast, we found that PIP$_2$ cortical structures are essentially independent of the

264 microtubule cytoskeleton, impaired here using *tba-2*(*RNAi*) (Fig. 4J, K). Overall, we

265 conclude that the formation of PIP$_2$ cortical structures depends on F-actin.

266

Lowering the cellular level of PIP$_2$ impacts F-actin distribution

We set out to address whether, conversely, PIP$_2$ regulates F-actin organization. If this were the case, then changing the level of PIP$_2$ lshould alter actomyosin network organization. We tested this prediction first by depleting PIP$_2$. To this end, we activated phospholipase C, an enzyme that cleaves PIP$_2$, by delivering Ionomycin and Ca^{2+} into *perm-1*(*RNAi*) embryos (Fig. S4A) (Hammond et al., 2012; Várnai and Balla, 1998). Cleavage of PIP$_2$ at the plasma membrane was monitored by the gradual loss of GFP::PH^{PLC1δ1} plasma membrane signal, which enabled us to determine, in each embryo, a comparable time t$_{1/2}$ when half of the initial GFP::PH^{PLC1δ1} plasma membrane fluorescence signal disappeared (Fig. S4B, C). A single plane in the middle of embryos expressing GFP::PH^{PLC1δ1} and Lifeact::mKate-2 was monitored in these experiments, as this proved most reliable for determining t$_{1/2}$. In doing so, we found that PIP$_2$ removal following addition of Ionomycin/ Ca^{2+} during pseudocleavage led to rapid alteration of embryo shape on the anterior side, coincident with altered F-actin organization (compare Fig. 5A and 5B, Fig. S4E). An analogous alteration in F-actin distribution was observed following Ionomycin/ Ca^{2+} addition during mitosis (Fig. 5C; Movie 7).

To test whether the shape change observed following Ionomycin/ Ca^{2+} addition is caused by alterations in F-actin organization, we combined this treatment with the actin depolymerizing agent Latrunculin A. As shown in Figure S4F and Movie 8, we found that this results in normally shaped embryos. Therefore, shape changes following PIP$_2$ removal are F-actin dependent. Together, these results uncover that a normal PIP$_2$ level is critical for the proper distribution of F-actin and thus for proper shape of the *C. elegans* zygote.

Increasing the cellular level of PIP$_2$ also impacts F-actin distribution

We sought to test the relationship between PIP$_2$ and F-actin further by increasing the level of PIP$_2$. We investigated whether this could be achieved by altering individual enzymes from the PIP$_2$ biosynthetic pathway using RNAi or mutant worms, but failed to find a single condition where this would be the case (see Table S1 for genes targeted in this study). Therefore, we set out to jointly inactivate OCRL-1 and UNC-26 for the following reasons (Fig. S4A). OCRL-1 is an inositol 5-phosphates that

299   hydrolyzes PIP_2 to phosphatidyl 4-phosphate (PIP), and whose depletion leads to

300   increased level of PIP_2 on *C. elegans* phagosomes (Cheng et al., 2015). Moreover,

301   UNC-26 is the *C. elegans* homologue of Synaptojanin, a polyphosphoinositide

302   phosphatase that can also hydrolyze PIP_2 to PIP, and whose impairment results in

303   vesicle trafficking defects and cytoskeletal abnormalities in the worm nervous system

304   (Charest et al., 1990; Harris et al., 2000).

305   We jointly depleted the function of these two PIP_2 phosphatases, using RNAi

306   for *ocrl-1* and an extant mutant for *unc-26*. Importantly, we found by comparing

307   cortical mCherry-PH$^{PLC1\delta1}$ mean intensity values that *ocrl-1*(*RNAi*) *unc-26*(*s1710*)

308   embryos exhibit an increased overall level of PIP_2 (Fig. S5A, B). Importantly, in

309   addition, we found that this leads to drastic alterations in PIP_2 and F-actin cortical

310   structures monitored by GFP::PH$^{PLC1\delta1}$ and Lifeact::mKate-2 (compared Fig. 5D and

311   Fig. 5E-F; Fig. S5C-H). First, in addition to motile PIP_2 structures, we found a

312   population of immotile PIP_2 clusters residing between the eggshell and the plasma

313   membrane (Fig. 5E, H, K, arrow; Fig. S5I, arrowhead), potentially corresponding to

314   PIP_2 boluses removed from the cell in an attempt to return to homeostatic conditions.

315   Second, we found that motile PIP_2 structures do not disappear as readily after

316   pseudocleavage as they do normally (Fig. 5H, I, compare to Fig. 5G; Fig. S5D).

317   Third, we found that motile PIP_2 structures exhibit altered distribution in all *ocrl-*

318   *1*(*RNAi*) *unc-26*(*s1710*) embryos (Fig. 5E, F; Fig. S5F, H). In some (hereafter referred

319   as class I embryos, N=27/48), the anterior movements of PIP_2 cortical structures and

320   of the actomyosin network do not stop at pseudocleavage, but instead continue until

321   the end of mitosis, resulting in a very small anterior domain of PIP_2 and F-actin

322   cortical structures (compare to Fig. 5G, J to Fig. 5H, K; Movie 9). In class II *ocrl-*

323   *1*(*RNAi*) *unc-26*(*s1710*) embryos (N=21/48), weak anteriorly directed movement of

324   cortical PIP_2 and F-actin is initiated, but both components become distributed

325   throughout the cortexby the end of the first cell cycle, except at the very posterior

326   (Fig. 5I, L). Whereas a clear cytokinesis furrow formed in all class 1 embryos, this

327   was the case in only 8/21 class 2 embryos; this subset exhibited more pronounced

328   anteriorly directed movements than the other 13. Overall, we conclude that the extent

329   of PIP_2 5-phosphatases depletion is stronger in class 2 than in class 1 embryos, with

330   the severe phenotype in the former perhaps reflecting an impact on multiple cellular

331   processes. Regardless, these findings establish that an increase in the level of PIP_2

332   as achieved in class 1 embryos leads to sustained cortical flows towards the anterior

11

333 side. Moreover, these results further demonstrate that PIP_2 regulates actin

334 cytoskeletal organization in one-cell *C. elegans* embryos.

335

336 **An appropriate level of PIP_2 is essential for proper PAR polarity establishment**

337 **and maintenance**

338 It is well known that the actomyosin network is essential for the establishment phase

339 of A-P polarization of the *C. elegans* zygote (Guo and Kemphues, 1996; Hill and

340 Strome, 1988; Hill and Strome, 1990; Munro et al., 2004; Severson and Bowerman,

341 2003; Shelton et al., 1999). Given that a proper level of PIP_2 is essential for correct

342 actomyosin network organization, we tested whether it is also important for A-P

343 polarity. To this end, we investigated the impact of excess PIP_2 on polarity using *ocrl-*

344 *1(RNAi) unc-26(s1710)* embryos expressing mCherry::PH$^{PLC1\delta1}$ and GFP::PAR-2 or

345 GFP::PAR-6, respectively (Fig. 6A-L). We found that the distribution of GFP::PAR-2

346 and GFP::PAR-6 domains changes in a manner consistent with alterations in motile

347 PIP_2 structures and the F-actin network, and this from early on (Movie 10). Thus, for

348 GFP::PAR-6, either a small domain formed on the very anterior (Fig. 6B, E; class 1,

349 N=5/9; Movie 10) or else the fusion protein remained present over the entire cortex,

350 except on the very posterior (Fig. 6C,F class 2; N=4/9). As expected, GFP::PAR-2

351 distributed in a reciprocal manner, either expanding drastically towards the anterior

352 (Fig. 6H, K; class 1, N=12/22; Movie 11) or else remaining restricted to the very

353 posterior (Fig. 6I, L; class 2, N=10/22). Together, these results indicate that a correct

354 level of PIP_2 is needed for proper F-actin network localization and, presumably as a

355 consequence, appropriate PAR polarity.

356   In the above experiments, the level of PIP_2 was in excess from the beginning

357 of development, such that one could not distinguish whether the impact on polarity

358 reflected a role strictly during the establishment phase or during both establishment

359 and maintenance phases. We reasoned that one could test specifically a potential

360 role for polarity maintenance by adding Ionomycin and Ca^{2+} to *perm-1(RNAi)*

361 embryos expressing mCherry::PH$^{PLC1\delta1}$ and GFP::PAR-2 after the establishment

362 phase. We found that the GFP::PAR-2 domain is unaltered at $t_{1/2}$ (compare Fig. 6M

363 and 6N, O), even though F-actin is already changed at that moment (see Fig. 5B, C).

364 Importantly, in addition, we found that the GFP::PAR-2 domain expands slowly

365 towards the anterior starting ~3 min thereafter (Fig. 6N, bottom two panels), with the

12

366   pseudocleavage furrow moving anteriorly initially, and then either retracting (Fig. 6M,

367   N; Movie 12, N=6/14), or else remaining at the very anterior until the end of the first

368   cell cycle Movie 13; N=8/14). Mirroring the findings at pseudocleavage, we found

369   that if $t_{1/2}$ occurs at nuclear envelope breakdown (NEBD), the GFP::PAR-2 domain

370   likewise expands slowly towards the anterior (Fig. 6O; Movie 14). Together these

371   results indicate that an appropriate level of PIP_2 is essential for proper PAR polarity

372   also during the maintenance phase.

373   In principle, PIP_2 could alter PAR polarity during the maintenance phase

374   through an impact on F-actin organization or else via an actin-independent role. A

375   potential role of F-actin in polarity maintenance is somewhat controversial, in contrast

376   to its well known role during polarity establishment (Goehring et al., 2011; Hill and

377   Strome, 1990; Liu and Fletcher, 2006; Severson and Bowerman, 2003). In the light of

378   our findings with PIP_2 level alterations, we set out to directly test whether F-actin

379   plays a role in polarity maintenance, first by adding Cytochalasin D to *perm-1*(*RNAi*)

380   embryos expressing Lifeact::mKate-2 and GFP::PAR-2, after polarity establishment

381   (Fig. 7A, B). Consistent with previous studies (Goehring et al., 2011; Hill and Strome,

382   1990), we found that Cytochalasin D addition at this stage does not alter the

383   GFP::PAR-2 domain in a major manner (Fig. 7A, B; Movie 15). However, we found

384   also that Cytochalasin D treatment does not fully disrupt F-actin, as clumps of

385   Lifeact::mKate-2 remain present on the embryo anterior (Fig. 7B). We hence turned

386   to inhibiting F-actin polymerization using Latrunculin A, which resulted in a total

387   depletion of F-actin (Fig. 7C; N=12; Movie 16). We observed membrane

388   invaginations that remove GFP::PAR-2 from the cortex into cytoplasmic aggregates

389   (Fig. 7C, arrowhead), as reported by others (Goehring et al., 2011; Redemann et al.,

390   2010). Importantly, in addition, we monitored changes in GFP::PAR-2 distribution not

391   as a function of drug addition time, as in earlier work (Goehring et al., 2011), but of

392   the time $t_{1/2}$ at which half of the Lifeact::mKate-2 fluorescence disappeared from the

393   membrane. In doing so, we found that the size of the GFP::PAR-2 domain decreased

394   significantly after $t_{1/2}$ in all embryos analyzed (Fig. 7C, bottom; N=12). As reported in

395   Figure S5J, we found that the $t_{1/2}$ of Lifeact::mKate-2 and of GFP::PAR-2

396   disappearance are highly correlated (Pearson coefficient ρ=0.86; p=0.0014). This

397   finding reinforces the conclusion that F-actin is critical not only for the establishment,

398   but also for the maintenance of PAR polarity.

13

399   Overall, we uncovered that a proper level of PIP_2 is essential for correct sizing

400   of PAR domains presumably through reorganization of F-actin, not only during

401   polarity establishment but also during polarity maintenance phase.

402

Discussion

403 In this work, we demonstrate that PIP_2 forms cortical structures in the one-cell *C.*

404 *elegans* embryo. We show that these structures depend on F-actin and, reciprocally,

405 that PIP_2 regulates F-actin organization, revealing an interdependence of these two

406 components in the worm zygote (Fig. 7D). Moreover, likely through its impact on the

407 actin cytoskeleton, PIP_2 is also needed for the correct sizing of anterior and posterior

408 PAR domains, demonstrating for the first time that a plasma membrane lipid

409 component participates in setting A-P polarity in the *C. elegans* embryo.

410

411

PIP_2 is present in discrete cortical structures in *C. elegans* zygotes

412 The distribution and dynamics of PIP_2 at the plasma membrane of early *C. elegans*

413 embryos were not clear prior to this work, primarily because the middle embryo plane

414 has been analyzed in most past investigations. Here, we developed cortical imaging

415 conditions to assay subcellular distributions at the cortex, the very location where the

416 function of PAR proteins and components critical for asymmetric division is exerted.

417 In doing so, we discovered that PIP_2 is present in dynamic polarized cortical

418 structures marked by the PIP_2 biomarker GFP::PH$^{PLC1\delta1}$, in line with recent

419 observations mentioning a non-uniform distribution of this fusion protein (Rodriguez

420 et al., 2017; Wang et al., 2017). Although patches of plasma membrane enriched in

421 PIP_2 have been observed in other systems (Chierico et al., 2015; Golub and Caroni,

422 2005; McLaughlin et al., 2002; Zhang et al., 2012), the stereotyped progression

423 through the first cell cycle of the large *C. elegans* zygote enabled us to uncover their

424 distribution and dynamics with unprecedented resolution. Why were such remarkable

425 structures not observed in previous studies in the worm? In addition to the fact that

426 they are not noticeable when imaging the middle plane of the embryo, other plausible

427 reasons include that PIP_2 cortical structures appear only transiently during the cell

428 cycle and that they are not preserved upon fixation (data not shown).

429 How do PIP_2 cortical structures assemble? We hypothesize that PIP_2 cortical

430 structures form by redistribution of existing PIP_2 rather than by *de novo* synthesis

431 through the PIP5K1 PPK-1, and this for two reasons. First, PIP_2 in other systems has

432 been suggested to diffuse much faster than it is synthesized (McLaughlin et al.,

433 2002), such that potential local synthesis is unlikely to dictate restricted PIP_2

435   localization. Second, PPK-1, the sole PIP5K1 in *C. elegans*, is enriched in the

436   posterior of the embryo (Panbianco et al., 2008), away from the location where most

437   PIP_2 cortical structures are. Interestingly, we find also that PIP_2 cortical structures

438   form and move independently of actomyosin contractions, as evidenced by their

439   unchanged presence and behavior upon NMY-2 depletion (data not shown).

440   Nevertheless, it remains possible that PIP_2 cortical structures form at membrane

441   protrusions or ruffles, which would be consistent with the finding that PIP_2 can

442   stimulate F-actin polymerization in curved but not in flat membranes (Gallop et al.,

443   2013), and with PIP_2 accumulating in membrane ruffles, nascent phagosomes and

444   the leading edge of motile cells (reviewed in McLaughlin et al., 2002; Zhang et al.,

445   2012). Overall, we propose that, in the *C. elegans* zygote, PIP_2 cortical structures

446   form through the redistribution of existing PIP_2 at the plasma membrane, perhaps

447   preferentially at membrane protrusions or ruffles.

448

449   **Interdependence of PIP_2 and F-actin**

450   PIP_2 and F-actin exhibit a reciprocal relationship in a number of systems, and we

451   uncover here that this is the case also in *C. elegans* embryos. We found that PIP_2

452   cortical structures and F-actin movements are coupled, with PIP_2 structures moving

453   slightly ahead of F-actin filaments, at velocities compatible with actin polymerization

454   driving their movements. This leads us to propose that actin polymerization pushes

455   PIP_2 cortical structures, in a manner reminiscent of other actin-dependent motility

456   processes such as that of *Listeria monocytogenes* (reviewed in Mogilner and Oster,

457   1996). While being pushed ahead of F-actin filaments in *C. elegans*, PIP_2 structures

458   might recruit factors promoting actin polymerization and branching, such as ECT-1,

459   RHO-1 and CDC-42, thus guiding proper F-actin network reorganization, in line with

460   suggestions in other systems (reviewed in Chichili and Rodgers, 2009). Intriguingly,

461   the distribution of a biosensor that detects active RhoA overlaps with that of NMY-2

462   foci (Reymann et al., 2016; Tse et al., 2012). Given that we show here that PIP_2

463   cortical structures do not overlap with NMY-2, while they do overlap with GFP::RHO-

464   1, perhaps the bulk of RHO-1 associating with PIP_2 cortical structures is not active.

465   Alternatively, given that we show here that RHO-1 colocalizes with its activating GEF

466   ECT-2, perhaps the RhoA biosensor used previously does not detected all active

467   RHO-1 species. Furthermore, it is interesting to note that non-muscle myosin 2 plays

16

468 a role in actin network disassembly in fish keratinocytes (Wilson et al., 2010).

469 Extrapolating from this observation, it is tempting to speculate that PIP_2, by promoting

470 F-actin assembly, and NMY-2, by promoting F-actin disassembly, in addition to its

471 role in network contractility, may together ensure proper F-actin dynamics in the early

472 *C. elegans* embryo.

473

PIP_2 and PAR-dependent polarity

474

475 PAR proteins are also distributed unevenly within their cortical domain. For instance,

476 PAR-6 exists in two cortical populations, one diffuse that depends on CDC-42, and

477 one punctate that colocalizes with PAR-3 (Beers and Kemphues, 2006; Robin et al.,

478 2014). Moreover, PAR-3 forms clusters that are crucial for proper polarity and that

479 assemble in a manner dependent on PCK-3, CDC-42, as well as actomyosin

480 contractility (Rodriguez et al., 2017; Wang et al., 2017). Intriguingly, we find that PIP_2

481 cortical structures colocalize within the more diffuse cortical PAR-6 protein

482 population, the one lacking PAR-3 (Beers and Kemphues, 2006; Robin et al., 2014;

483 Rodriguez et al., 2017; Wang et al., 2017). We establish here that increasing the

484 level of PIP_2 augments the segregation of both PAR-6 populations to the embryo

485 anterior, potentially because cortical clustering of PAR-3 depends on the actomyosin

486 cytoskeleton and cortical tension (Beers and Kemphues, 2006; Robin et al., 2014;

487 Rodriguez et al., 2017; Wang et al., 2017). Overall, we propose that increasing the

488 level of PIP_2 might augment cortical tension, which could in turn promote PAR-3

489 clustering and thereby aid segregation.

490   We show that a correct PIP_2 level is essential for proper polarity establishment

491 and maintenance trough correct positioning of GFP::PAR-2 and GFP::PAR-6

492 domains. When increasing the level of PIP_2, the continued movement of PAR

493 domains towards the anterior until the end of mitosis alters their relative size. This is

494 reminiscent of changes in the size of PAR domains that occur upon RGA-3/4

495 depletion (Schonegg et al., 2007). However, although *rga-3/4*(*RNAi*) embryos exhibit

496 a hypercontractile actomyosin network, this is not the case of embryos with increased

497 PIP_2 level. We thus propose that actomyosin contractility regulated by NMY-2 and F-

498 actin organization regulated by PIP_2 contribute in concert to correct movements of the

499 actomyosin network, and, therefore, proper sizing of PAR-polarity domains.

500

On the role of the actomyosin network in polarity establishment and maintenance

503 The actomyosin network plays a well-established role during polarity establishment,
504 whereas its role during polarity maintenance has been less clear (Goehring et al.,
505 2011; Hill and Strome, 1990; Liu and Fletcher, 2006; Severson and Bowerman,
506 2003). Our results, together with that of others, indicate that the actomyosin network
507 regulates the size and localization of PAR domains in two ways. First, when the
508 actomyosin network moves along the A-P embryonic axis, PAR domains alter their
509 distribution accordingly. This relationship was clear prior to this work for the polarity
510 establishment phase, and we show here that this is also the case during polarity
511 maintenance. Second, actin has been suggested to play merely a passive role during
512 the maintenance phase in preventing cortical PAR-2 removal through membrane
513 invaginations driven by microtubules (Goehring *et al.,* 2011). We reveal here that the
514 lack of this function can lead to the near total disappearance of cortical PAR-2,
515 emphasizing the critical importance of actin also during the maintenance phase.

516 Overall, our results in the *C. elegans* zygote are consistent with the role of
517 PIP_2 in F-actin reorganization and polarity in other organisms. Previous work in *C.*
518 *elegans* showed that depletion of CSNK-1, which negatively regulates PPK-1
519 localization, does not influence polarity at the end of the first cell cycle (Panbianco et
520 al., 2008). Perhaps PPK-1 distribution plays only a minor role in regulating the
521 cellular level of PIP_2 in the zygote, being dispensable for PIP_2 cortical structure
522 formation. In this case, depleting an enzyme such as CSNK-1 that negatively
523 regulates PPK-1 localization would not be expected to influence PIP_2 cortical
524 distribution. Here, by contrast, we establish unequivocally that alterations in the level
525 of PIP_2 impairs polarity establishment and maintenance during the first asymmetric
526 division of *C. elegans* embryos.

527

528

18

Material and Methods

Worm Strains

Nematodes were maintained at 24°C using standard protocols (Brenner, 1974). The following worm strains were used: GFP::PH$^{PLC1\delta1}$ (OD58, *unc-119*(*ed3*) III; ltIs38[*pie-1*p::GFP::PH(PLC1delta1) + *unc-119*(+)]) (Audhya et al., 2005); mCherry::PH$^{PLC1\delta1}$ (OD70, *unc-119*(*ed3*) III; ltIs44[*pie-1*p::mCherry::PH(PLC1delta1) + *unc-119*(+)]V) (Audhya et al., 2005); GFP::PAR-2 (TH129) and GFP::PAR-6 (TH110) (Schonegg et al., 2007); GFP::NMY-2 (LP162, *nmy-2*(*cp13*[*nmy-2*::gfp + LoxP]) I) (Dickinson et al., 2013); CAV-1::GFP (RT688, unc-119(ed3) III; pwIs281[CAV-1::GFP, *unc-119*(+)]) (Sato et al., 2006); mNeonGreen::PH$^{PLC1\delta1}$ (LP274, cpIs45[P*mex-5*::mNeonGreen::PLCδ-PH::*tbb-2* 3'UTR + *unc-119*(+)] II; *unc-119*(*ed3*) III), mKate-2::PH$^{PLC1\delta1}$ (LP307, cpIs54[P*mex-5*::mKate2::PLCδ-PH(A735T)::*tbb-2* 3'UTR + *unc-119*(+)] II; *unc-119*(ed3) III) and mCherry::PH$^{PLC1\delta1}$ (LP308, cpIs55[P*mex-5*::mCherry-C1::PLCδ-PH::*tbb-2* 3'UTR + *unc-119*(+)] II; *unc-119*(ed3) III) (Heppert et al., 2016); Lifeact::mKate-2 (strain SWG001) (Reymann et al., 2016); GFP::RHO-1 (SA115, *unc-119*(*ed3*) III; tjIs1[*pie-1*::GFP::*rho-1* + *unc-119*(+)]) (Motegi et al., 2006); GFP::CDC-42 (SA131, *unc-119*(*ed3*) III; tjIs6[*pie-1*p::GFP::*cdc-42* + *unc-119*(+)].) (Motegi and Sugimoto, 2006); GFP::ECT-2 (SA125, unc-119(ed3) III; tjIs4[*pie-1*::GFP::*ect-2* + *unc-119*(+)]) (Motegi and Sugimoto, 2006); *unc-26*(*s1710*) (EG3027, *unc-26*(*s1710*) IV) (Charest et al., 1990); *age-1*(*m333*), (DR722, *age-1*(*m333*)/mnC1 *dpy-10*(*e128*) *unc-52*(*e444*) II) (Riddle, 1988). Crosses of worm strains were performed at 20°C to generate lines homozygote for all transgenes, which were then maintained at 24°C. For GFP::RHO-1 and mCherry::PH$^{PLC1\delta1}$, as well as GFP::PH$^{PLC1\delta1}$ and Lifeact::mKate-2, worm lines were crossed and F1 progeny heterozygote for both transgenes imaged.

RNAi

RNAi-mediated deletion was performed essentially as described (Kamath et al., 2001), using bacterial feeding strains either from the Ahringer (Kamath et al., 2003) or the Vidal library (Rual et al., 2004) (gift from Jean-François Rual and Marc Vidal). RNAi for *par-2* (Ahringer), *par-3* (Ahringer), *nmy-2* (Ahringer), *act-1* (Vidal), *tba-2* (Vidal), and *ocrl-1* (Ahringer) was performed by feeding L3-L4 animals with bacteria expressing the corresponding dsRNA at 24°C for 20-26 hours. RNAi for *perm-1* (Ahringer) was performed by feeding L4 and young adults with bacteria expressing

19

562   *perm-1* dsRNA at 20°C for 12-18 hours. The effectiveness of the deletion was

563   screened phenotypically as follows: *par-2*(*RNAi*) and *par-3*(*RNAi*) -symmetric spindle

564   positioning and cell division; *nmy-2*(*RNAi*) and *act-1*(*RNAi*) -absence of cortical

565   ruffles, symmetric spindle positioning, no cytokinesis; *tba-2*(*RNAi*) -defective

566   pronuclear meeting, no centration/rotation, no spindle assembly, misplaced

567   cytokinesis furrow specification; *ocrl-1*(*RNAi*) -see results, *perm-1*(*RNAi*): successful

568   action of added drug.

Live imaging

570   Gravid hermaphrodites were dissected in osmotically balanced blastomere culture

571   medium (Shelton and Bowerman, 1996) and the resulting embryos mounted on a 2%

572   agarose pad. DIC time lapse microscopy (Fig. 1A,C,E,G,I) was performed at 25°C ±

573   1°C with a 100× (NA 1.25 Achrostigmat) objective and standard DIC optics on a

574   Zeiss Axioskop 2 microscope. All other images were acquired using an inverted

575   Olympus IX 81 microscope equipped with a Yokogawa spinning disk CSU - W1 with

576   a 63 (NA 1.42 U PLAN S APO) objective and a 16-bit PCO Edge sCMOS camera at

577   23°C. Images were obtained using 488 nm and 561 nm solid-state lasers with an

578   exposure time of 400 ms and a laser power of 20-60%. For cortical imaging, 3 planes

579   at the cell cortex (each 0.25 μm apart) were acquired. Cell cycle stages were

580   determined using transmission light microscopy by imaging the middle plane in

581   parallel (data not shown).

Image processing and analysis

583   Cortical images of GFP::PH$^{PLC1\delta1}$ used for quantification were processed as follows:

584   the 3 cortical planes were z-projected using average intensity projection, then a

585   median filter of 1 pixel was applied. The background of the entire image was

586   subtracted using the measured mean background in each frame. Signal intensity

587   decay due to photobleaching was corrected with the Fiji plugin "bleach correction"

588   using the exponential fitting method. The entire cortical region was segmented by

589   applying a binary automated histogram-based threshold, followed by iterated

590   morphological operations. Cortical structures were segmented by applying a binary

591   intensity threshold, calculated by fitting the pixel intensity histogram with a Gaussian

592   function and setting the threshold at 4 sigma from the Gaussian peak. The size of

593   cortical structures was normalized to the total cortical area.

594   Curves of normalized cortical structures sizes were fit with a sigmoidal model and

595   synchronized, setting the sigmoid inflection point, which corresponded typically to the

596   time of centration/rotation, as time t=0 s. Curves of normalized cortical structures

597   sizes were aligned manually for *act-1*(*RNAi*) and *unc-26*(*s1710*) *ocrl-1*(*RNAi*)

598   embryos using the clear landmark provided by Nuclear Envelope Breakdown (NEDB)

599   as a reference, because a sigmoid function could not be fit with the PH markers in

600   these cases. Since the time separating centration/rotation from NEDB is typically150

601   seconds, t=0 was set at -150 seconds prior to NEDB for *act-1*(*RNAi*) and *unc-*

602   *26*(*s1710*) *ocrl-1*(*RNAi*) embryos.

603   The Elongation Index was calculated as follows: $((\text{perimeter}^2)/\text{area})/4\pi$ using the

604   MATLAB image processing function "regionprops". We then normalized the

605   Elongation Index by a factor of $1/\pi$ such that a square of 2 x 2 pixels has an

606   Elongation Index of 1.

607   Cortical images obtained by live confocal spinning disk imaging and shown in the

608   figures were processed as follows: the 3 cortical planes were z-projected using

609   maximum intensity projection, then a median filter of 1 was applied. The grey value

610   fluorescence intensity of some transgenes (GFP::PH$^{PLC1\delta1}$ as heterozygote,

611   GFP::PAR-2, GFP::PAR-6, Lifeact::mKate-2, mNeonGreen-PH$^{PLC1\delta1}$) was slightly

612   variable likely resulting from variable expression/folding of the fluorescent fusion

613   protein, which may stem for several reasons, including F1 heterozygosity,

614   temperature shifting, silencing during crossing. The brightness and contrast of

615   images resulting from embryos expressing these transgenes was therefore adjusted

616   accordingly. The fluorescence intensity of mCherry::PH$^{PLC1\delta1}$ was also variable in

617   some cases; therefore, the brightness and contrast of images from embryos

618   expressing mCherry::PH$^{PLC1\delta1}$ were therefore adjusted accordingly as well. Such

619   variability was especially pronounced in UNC-26 and OCRL-1 depleted embryos. To

620   compare the intensity of mCherry-PH$^{PLC1\delta1}$ in control embryos and *unc-26*(*s1710*)

621   *ocrl-1*(*RNAi*) embryos, 3 cortical planes, acquired as described above, were z-

622   projected by summing the intensity of all slices. The resulting mean intensities were

623   then computed as follows. First, a Otsu threshold was used to retrieve the brightest

624   elements - including the embryo - of the image, retaining only the biggest blob,

625   corresponding to the embryo. Values outside the embryo were averaged to obtain

626   the mean background intensity value, which was subtracted from the embryo pixels.

21

627 Thereafter, embryo pixel values were averaged to obtain the mean pixel intensity

628 value.

629 **Cortical flow measurement, correlation analysis, and PIP$_2$ structures tracking**

630 For Particle Image Velocimetry (PIV) analysis, cortical image sequences of

631 mNeonGreen::PH$^{PLC1\delta1}$ and Lifeact::mKate-2 were prepared by performing a

632 maximum intensity z-projection of a stack of 2 planes (0.25 µm apart) and applying a

633 median filer of 1 pixel. PIP$_2$ cortical structures and the F-actin network were then

634 segmented using the following procedure: the embryo was first extracted from the

635 background using a histogram-based automated threshold, keeping only blobs of a

636 size superior to one third of the biggest blob. The resulting binary images were

637 deemed to be the embryo area. We applied a morphological erosion to the

638 mNeonGreen::PH$^{PLC1\delta1}$ movies with a large structuring element (a disk 30 pixels in

639 radius) to calculate the average value of the pixels not corresponding to PIP$_2$ cortical

640 structures; the PIP$_2$ cortical structures were then segmented as the pixels of intensity

641 higher than the computed average value, times a scaling factor determined

642 empirically (1.7). The extraction of the F-actin network was achieved simply by

643 determining a histogram-based automated threshold on the morphological top-hat of

644 the F-actin image. F-actin filaments and PIP$_2$ cortical structures where segmented

645 prior to PIV analysis to ensure that only flow fields in the region of interest are

646 measured.

647 PIV was then performed to measure cortical flows using the MATLAB based PIVlab

648 toolbox (Thielicke and Stamhuis, 2014); this splits each image of a movie into a

649 regular grid, for which the size of grid cells is given by the user. The position of each

650 cell in the next image is estimated by finding the maximum normalized cell-to-cell

651 cross-correlation of equivalent sizes in a geometrical neighborhood called

652 interrogation area. PIV was applied to mNeonGreen::PH$^{PLC1\delta1}$ and Lifeact::mKate-2

653 separately, after segmentation of the corresponding cortical structures. The choice of

654 the sizes of the cells and interrogation areas was a balance between two criteria:

655 smaller cells allow to compute displacements with high spatial resolution, but

656 excessively small cells do not contain enough information to be reliably correlated to

657 other cells; the estimation of displacements of bigger cells is hence more reliable, but

658 are computed with lesser resolution. We found empirically that 32 x 32 pixels for cell

659 sizes, and 64 x 64 pixels for interrogation areas, to be a good compromise.

660   The PIV velocity fields output for both mNeonGreen::PH$^{PLC1\delta1}$ and Lifeact::mKate-2

661   signals were compared in terms of angles between colocalized features and

662   correlation of the norms. For each movie, angles between velocity vectors of

663   colocalized features were computed and plotted on a histogram. The average angle

664   value for each time point and each movie was also computed, so as to monitor the

665   coherence between the two vector fields over time. Similarly, we computed the

666   correlations of the norms of all velocities in the two movies, for the whole movies, and

667   also time-wise. The cut-off angle is defined as the $\theta 0$ parameter of the curve of

668   equation $y = a \exp(-\theta/\theta 0)$ fitted to the histogram.

669   Cross-correlation analysis was performed as follows. Movies used to calculate the

670   cross-correlation were acquired alternating acquisition of red or green channel first to

671   prevent introducing a bias through the order of image acquisition. The colocalization

672   of the thresholded PIP$_2$ cortical structures and F-actin network for a variety of time

673   shifts was computed considering a time shift Δt (positive or negative), the

674   colocalization of the segmented PIP$_2$ image at time t and the segmented F-actin

675   image at time t-Δt using the following formula:

676   Colocalization = (PIP$_2$(t) $\cap$ F-actin(t-Δt)/ PIP$_2$ (t)

677   Colocalization was computed in this manner from Δt = -(T-1) to Δt = (T-1), where T is

678   the total duration of the movie. The Δt for which colocalization is maximal represents

679   the time shift between PIP$_2$ and F-actin. The mean time shift and its error were

680   computed as follows: we fitted a parabola of equation $y = a + (t-t0)^2 + b$ to the

681   location correlation as a function of the time shift. We calculated the best a, b and t0

682   parameters using a least-squares method, and input the standard deviations of the

683   correlations to create a weight matrix used during the adjustment. The results were

684   the mean time shift t0 = 9.3s and the standard deviation sigma_t0 = 1.5s.

685   To track PIP$_2$ structures, embryos expressing mNG-PH$^{PLC1\delta1}$ were imaged with an

686   exposure time of 50 ms, laser power of 60% and 70 ms frame rate. PIP$_2$ structures

687   were tracked manually on maximum intensity z-projection of the images containing

688   the moving PIP$_2$ structures of interest. The length of the track was obtained by

689   reslicing it using the Fiji plugin "Reslice". Velocity was calculated from the

690   corresponding number of time points and track length.

23

Drug addition

The eggshell was permeabilized by performing *perm-1*(*RNAi*) as described above. Gravid hermaphrodites were dissected in a cell culture dish with a glass bottom, and the resulting embryos imaged with an inverted confocal spinning disk microscope (see above). Drugs were added under the microscope while imaging to precisely control the timing of drug addition. The following drugs and concentrations were utilized: 30 µM Ionomycin (Calbiochem, 407950), 3-5 mM $CaCl_2$ (Sigma-Aldrich, C5080), 20 µM Cytochalasin D (AppliChem, 22144-77-0), 12.5 µM Latrunculin A (Sigma-Aldrich, 76343-93-6). For control movies, DMSO at a concentration equivalent to the final DMSO concentration in the drug solutions was added to the buffer prior to dissection.

Successful drug action was determined for each embryo by the disappearance of the $PH^{PLC1\delta1}$ fluorescence signal from the plasma membrane (Ionomycin/ Ca^{2+}, Latrunculin A) and of Lifeact::mKate-2 from the cell cortex (Latrunculin A, Cytochalasin D). The time between drug addition and drug action was variable, probably due to variations in eggshell permeability upon *perm-1*(*RNAi*). As a comparable reference time between embryos, we therefore determined the time $t_{1/2}$ (t inflection) when half of fluorescence at the plasma membrane has disappeared. $t_{1/2}$ was determined as follows: the total cortical region of the embryo was segmented by applying a binary automated histogram-based threshold. Fluorescent values at a distance of 20 pixels from the edge were measured, and their mean fluorescence values plotted over time; the inflection point of a fitted sigmoid function was then determined as $t_{1/2}$.

Lipid delivery

BODIPY® FL Phosphatidylinositol 4,5-bisphosphate (Echelon Bioscience, C-45F6) (end concentration: 2 µM) was delivered to *perm-1*(*RNAi*) embryos by adding it to the buffer in which gravid worms were dissected. It typically helped to premix BODIPY® FL Phosphatidylinositol 4,5-bisphosphate (100 µM) with a carrier histone (P-9C2; Echelon Bioscience) (300 µM) (Ozaki et al., 2000). Phosphoinositide-histone complexes were formed as described (Kotak et al., 2014): both components were mixed by vigorous vortexing and then incubated for at 15 min at room temperature.

24

722 **Statistical analyses**

723 The software package JMP 13.2.0 (SAS Institute GmbH) and MATLAB 2016 were

724 used to perform statistical analysis. Two-group comparisons were performed using

725 Student's t-test. Results with values of $p \leq 0.05$ were considered statistically

726 significant.

Acknowledgments

References

Audhya, A., Hyndman, F., McLeod, I. X., Maddox, A. S., Yates, J. R., Desai, A. and Oegema, K. (2005). A complex containing the Sm protein CAR-1 and the RNA helicase CGH-1 is required for embryonic cytokinesis in Caenorhabditis elegans. *J. Cell Biol.* **171**, 267–79.

Beers, M. and Kemphues, K. (2006). Depletion of the co-chaperone CDC-37 reveals two modes of PAR-6 cortical association in C. elegans embryos. *Development* **133**, 3745–3754.

Bienkowska, D. and Cowan, C. R. (2012). Centrosomes Can Initiate a Polarity Axis from Any Position within One-Cell C. elegans Embryos. *Curr. Biol.* **22**, 583–589.

Blanchoud, S., Budirahardja, Y., Naef, F. and Gönczy, P. (2010). ASSET: A robust algorithm for the automated segmentation and standardization of early Caenorhabditis elegans embryos. *Dev. Dyn.* **239**, 3285–3296.

Brangbour, C., du Roure, O., Helfer, E., Démoulin, D., Mazurier, A., Fermigier, M., Carlier, M.-F., Bibette, J. and Baudry, J. (2011). Force-Velocity Measurements of a Few Growing Actin Filaments. *PLoS Biol.* **9**, e1000613.

Brenner, S. (1974). The genetics of Caenorhabditis elegans. *Genetics* **77**, 71–94.

Brown, D. A. (2015). PIP2Clustering: From model membranes to cells. *Chem. Phys. Lipids* **192**, 33–40.

Cameron, L. A., Giardini, P. A., Soo, F. S. and Theriot, J. A. (2000). Secrets of actin-based motility revealed by a bacterial pathogen. *Nat. Rev. Mol. Cell Biol.* **1**, 110–119.

Carlsson, A. E. (2003). Growth velocities of branched actin networks. *Biophys. J.* **84**, 2907–18.

Carlsson, A. E. (2010). Actin dynamics: from nanoscale to microscale. *Annu. Rev. Biophys.* **39**, 91–110.

Carvalho, A., Olson, S. K., Gutierrez, E., Zhang, K., Noble, L. B., Zanin, E., Desai, A., Groisman, A. and Oegema, K. (2011). Acute Drug Treatment in the Early C. elegans Embryo. *PLoS One* **6**, e24656.

769 **Charest, D. L., Clark, D. V, Green, M. E. and Baillie, D. L.** (1990). Genetic and fine
770   structure analysis of unc-26(IV) and adjacent regions in Caenorhabditis elegans.
771   *Mol. Gen. Genet.* **221**, 459–65.

772 **Cheng, S., Wang, K., Zou, W., Miao, R., Huang, Y., Wang, H. and Wang, X.**
773   (2015). PtdIns(4,5)P $_2$ and PtdIns3P coordinate to regulate phagosomal sealing
774   for apoptotic cell clearance. *J. Cell Biol.* **210**, 485–502.

775 **Chichili, G. R. and Rodgers, W.** (2009). Cytoskeleton–membrane interactions in
776   membrane raft structure. *Cell. Mol. Life Sci.* **66**, 2319–2328.

777 **Chierico, L., Joseph, A. S., Lewis, A. L. and Battaglia, G.** (2015). Live cell imaging
778   of membrane / cytoskeleton interactions and membrane topology. *Sci. Rep.* **4**,
779   6056.

780 **Claret, S., Jouette, J., Benoit, B., Legent, K. and Guichet, A.** (2014). PI(4,5)P2
781   produced by the PI4P5K SKTL controls apical size by tethering PAR-3 in
782   Drosophila epithelial cells. *Curr. Biol.* **24**, 1071–9.

783 **Cowan, C. R. and Hyman, A. A.** (2004). Centrosomes direct cell polarity
784   independently of microtubule assembly in C. elegans embryos. *Nature* **431**, 92–
785   96.

786 **Cuenca, A. A., Schetter, A., Aceto, D., Kemphues, K. and Seydoux, G.** (2003).
787   Polarization of the C. elegans zygote proceeds via distinct establishment and
788   maintenance phases. *Development* **130**, 1255–65.

789 **De Craene, J.-O., Bertazzi, D., Bär, S. and Friant, S.** (2017). Phosphoinositides,
790   Major Actors in Membrane Trafficking and Lipid Signaling Pathways. *Int. J. Mol.*
791   *Sci.* **18**, 634.

792 **Di Paolo, G. and De Camilli, P.** (2006). Phosphoinositides in cell regulation and
793   membrane dynamics. *Nature* **443**, 651–657.

794 **Dickinson, D. J., Ward, J. D., Reiner, D. J. and Goldstein, B.** (2013). Engineering
795   the Caenorhabditis elegans genome using Cas9-triggered homologous
796   recombination. *Nat. Methods* **10**, 1028–34.

797 **Entchev, E. V and Kurzchalia, T. V** (2005). Requirement of sterols in the life cycle
798   of the nematode Caenorhabditis elegans. *Semin. Cell Dev. Biol.* **16**, 175–82.

28

799 **Gallop, J. L., Walrant, A., Cantley, L. C. and Kirschner, M. W.** (2013).
800   Phosphoinositides and membrane curvature switch the mode of actin
801   polymerization via selective recruitment of toca-1 and Snx9. *Proc. Natl. Acad.*
802   *Sci.* **110**, 7193–7198.

803 **Garcia, P., Gupta, R., Shah, S., Morris, A. J., Rudge, S. A., Scarlata, S., Petrova,**
804   **V., McLaughlin, S. and Rebecchi, M. J.** (1995). The pleckstrin homology
805   domain of phospholipase C-.delta.1 binds with high affinity to
806   phosphatidylinositol 4,5-bisphosphate in bilayer membranes. *Biochemistry* **34**,
807   16228–16234.

808 **Gervais, L., Claret, S., Januschke, J., Roth, S. and Guichet, A.** (2008). PIP5K-
809   dependent production of PIP2 sustains microtubule organization to establish
810   polarized transport in the Drosophila oocyte. *Development* **135**, 3829–3838.

811 **Goehring, N. W., Hoege, C., Grill, S. W. and Hyman, A. A.** (2011). PAR proteins
812   diffuse freely across the anterior–posterior boundary in polarized C. elegans
813   embryos. *J. Cell Biol.* **193**,.

814 **Goldstein, B. and Macara, I. G.** (2007). The PAR Proteins: Fundamental Players in
815   Animal Cell Polarization. *Dev. Cell* **13**, 609–622.

816 **Golub, T. and Caroni, P.** (2005). PI(4,5)P2-dependent microdomain assemblies
817   capture microtubules to promote and control leading edge motility. *J. Cell Biol.*
818   **169**, 151–65.

819 **Golub, T. and Pico, C.** (2005). Spatial control of actin-based motility through
820   plasmalemmal PtdIns (4, 5) P2-rich raft assemblies. *Biochem. Soc. Symp.*

821 **Gönczy, P.** (2008). Mechanisms of asymmetric cell division: flies and worms pave
822   the way. *Nat. Rev. Mol. Cell Biol.* **9**, 355–366.

823 **Guglielmi, G., Barry, J. D., Huber, W. and De Renzis, S.** (2015). An Optogenetic
824   Method to Modulate Cell Contractility during Tissue Morphogenesis. *Dev. Cell*
825   **35**, 646–60.

826 **Guo, S. and Kemphues, K. J.** (1996). A non-muscle myosin required for embryonic
827   polarity in Caenorhabditis elegans. *Nature* **382**, 455–458.

828 **Hammond, G. R. V., Fischer, M. J., Anderson, K. E., Holdich, J., Koteci, A.,**

29

829   **Balla, T. and Irvine, R. F.** (2012). PI4P and PI(4,5)P2 Are Essential But
830   Independent Lipid Determinants of Membrane Identity. *Science (80-.).* **337**,.

831 **Hao, Y., Boyd, L. and Seydoux, G.** (2006). Stabilization of cell polarity by the C.
832   elegans RING protein PAR-2. *Dev. Cell* **10**, 199–208.

833 **Harris, T. W., Hartwieg, E., Horvitz, H. R. and Jorgensen, E. M.** (2000). Mutations
834   in synaptojanin disrupt synaptic vesicle recycling. *J. Cell Biol.* **150**, 589–600.

835 **Heppert, J. K., Dickinson, D. J., Pani, A. M., Higgins, C. D., Steward, A.,**
836   **Ahringer, J., Kuhn, J. R. and Goldstein, B.** (2016). Comparative assessment
837   of fluorescent proteins for in vivo imaging in an animal model system. *Mol. Biol.*
838   *Cell* **27**, 3385–3394.

839 **Hill, D. P. and Strome, S.** (1988). An analysis of the role of microfilaments in the
840   establishment and maintenance of asymmetry in Caenorhabditis elegans
841   zygotes. *Dev. Biol.* **125**, 75–84.

842 **Hill, D. P. and Strome, S.** (1990). Brief cytochalasin-induced disruption of
843   microfilaments during a critical interval in 1-cell C. elegans embryos alters the
844   partitioning of developmental instructions to the 2-cell embryo. *Development*
845   **108**, 159–72.

846 **Hoege, C. and Hyman, A. A.** (2013). Principles of PAR polarity in Caenorhabditis
847   elegans embryos. *Nat. Rev. Mol. Cell Biol.* **14**, 315–322.

848 **Johnson, J. L., Erickson, J. W. and Cerione, R. A.** (2012). C-terminal Di-arginine
849   Motif of Cdc42 Protein Is Essential for Binding to Phosphatidylinositol 4,5-
850   Bisphosphate-containing Membranes and Inducing Cellular Transformation. *J.*
851   *Biol. Chem.* **287**, 5764–5774.

852 **Kamath, R. S., Martinez-Campos, M., Zipperlen, P., Fraser, A. G. and Ahringer,**
853   **J.** (2001). Effectiveness of specific RNA-mediated interference through ingested
854   double-stranded RNA in Caenorhabditis elegans. *Genome Biol.* **2**,
855   RESEARCH0002.

856 **Kamath, R. S., Fraser, A. G., Dong, Y., Poulin, G., Durbin, R., Gotta, M., Kanapin,**
857   **A., Le Bot, N., Moreno, S., Sohrmann, M., et al.** (2003). Systematic functional
858   analysis of the Caenorhabditis elegans genome using RNAi. *Nature* **421**, 231–
859   237.

860   **Kirby, C., Kusch, M. and Kemphues, K.** (1990). Mutations in the par genes of
861   Caenorhabditis elegans affect cytoplasmic reorganization during the first cell
862   cycle. *Dev. Biol.* **142**, 203–15.

863   **Knoblich, J. A.** (2010). Asymmetric cell division: recent developments and their
864   implications for tumour biology. *Nat. Rev. Mol. Cell Biol.* **11**, 849–860.

865   **Kotak, S., Busso, C. and Gonczy, P.** (2014). NuMA interacts with phosphoinositides
866   and links the mitotic spindle with the plasma membrane. *EMBO J.* **33**, 1815–
867   1830.

868   **Krahn, M. P., Klopfenstein, D. R., Fischer, N. and Wodarz, A.** (2010). Membrane
869   Targeting of Bazooka/PAR-3 Is Mediated by Direct Binding to Phosphoinositide
870   Lipids. *Curr. Biol.* **20**, 636–642.

871   **Kumfer, K. T., Cook, S. J., Squirrell, J. M., Eliceiri, K. W., Peel, N., O'Connell, K.**
872   **F. and White, J. G.** (2010). CGEF-1 and CHIN-1 Regulate CDC-42 Activity
873   during Asymmetric Division in the Caenorhabditis elegans Embryo. *Mol. Biol.*
874   *Cell* **21**, 266–277.

875   **Kurzchalia, T. V and Ward, S.** (2003). Why do worms need cholesterol? *Nat. Cell*
876   *Biol.* **5**, 684–8.

877   **Kurzchalia, T. V., Scheel, J., Srinivasan, J., Honnert, U. and Henske, A.** (1999).
878   Involvement of caveolin-1 in meiotic cell-cycle progression in Caenorhabditis
879   elegans. *Nat. Cell Biol.* **1**, 127–129.

880   **Lemmon, M. A., Ferguson, K. M., O'Brien, R., Sigler, P. B. and Schlessinger, J.**
881   (1995). Specific and high-affinity binding of inositol phosphates to an isolated
882   pleckstrin homology domain. *Proc. Natl. Acad. Sci. U. S. A.* **92**, 10472–6.

883   **Liu, A. P. and Fletcher, D. A.** (2006). Actin polymerization serves as a membrane
884   domain switch in model lipid bilayers. *Biophys. J.* **91**, 4064–70.

885   **McLaughlin, S., Wang, J., Gambhir, A. and Murray, D.** (2002). PIP$_2$ and Proteins:
886   Interactions, Organization, and Information Flow. *Annu. Rev. Biophys. Biomol.*
887   *Struct.* **31**, 151–175.

888   **Merris, M., Wadsworth, W. G., Khamrai, U., Bittman, R., Chitwood, D. J. and**
889   **Lenard, J.** (2003). Sterol effects and sites of sterol accumulation in

31

890   Caenorhabditis elegans: developmental requirement for 4alpha-methyl sterols. *J.*
891   *Lipid Res.* **44**, 172–81.

892   **Mogilner, A. and Oster, G.** (1996). Cell Motility Driven by Actin Polymerization.
893   *Biophys. J.* **71**, 3030–3045.

894   **Motegi, F. and Sugimoto, A.** (2006). Sequential functioning of the ECT-2 RhoGEF,
895   RHO-1 and CDC-42 establishes cell polarity in Caenorhabditis elegans embryos.
896   *Nat. Cell Biol.* **8**, 978–985.

897   **Motegi, F., Velarde, N. V., Piano, F., Sugimoto, A., Malone, C. J., White, J.,**
898   **Seydoux, G., Saxton, W. and Salmon, E. D.** (2006). Two Phases of Astral
899   Microtubule Activity during Cytokinesis in C. elegans Embryos. *Dev. Cell* **10**,
900   509–520.

901   **Motegi, F., Zonies, S., Hao, Y., Cuenca, A. A., Griffin, E. and Seydoux, G.** (2011).
902   Microtubules induce self-organization of polarized PAR domains in
903   Caenorhabditis elegans zygotes. *Nat. Cell Biol.* **13**, 1361–1367.

904   **Munro, E., Nance, J. and Priess, J. R.** (2004). Cortical Flows Powered by
905   Asymmetrical Contraction Transport PAR Proteins to Establish and Maintain
906   Anterior-Posterior Polarity in the Early C. elegans Embryo. *Dev. Cell* **7**, 413–424.

907   **Ozaki, S., DeWald, D. B., Shope, J. C., Chen, J. and Prestwich, G. D.** (2000).
908   Intracellular delivery of phosphoinositides and inositol phosphates using
909   polyamine carriers. *Proc. Natl. Acad. Sci. U. S. A.* **97**, 11286–91.

910   **Pacquelet, A.** (2017). Asymmetric Cell Division in the One-Cell C. elegans Embryo:
911   Multiple Steps to Generate Cell Size Asymmetry.pp. 115–140. Springer, Cham.

912   **Panbianco, C., Weinkove, D., Zanin, E., Jones, D., Divecha, N., Gotta, M. and**
913   **Ahringer, J.** (2008). A casein kinase 1 and PAR proteins regulate asymmetry of
914   a PIP(2) synthesis enzyme for asymmetric spindle positioning. *Dev. Cell* **15**,
915   198–208.

916   **Redemann, S., Pecreaux, J., Goehring, N. W., Khairy, K., Stelzer, E. H. K.,**
917   **Hyman, A. A. and Howard, J.** (2010). Membrane Invaginations Reveal Cortical
918   Sites that Pull on Mitotic Spindles in One-Cell C. elegans Embryos. *PLoS One* **5**,
919   e12301.

920 **Reymann, A.-C., Staniscia, F., Erzberger, A., Salbreux, G. and Grill, S. W.** (2016).
921 Cortical flow aligns actin filaments to form a furrow. *Elife* **5**,.

922 **Riddle, D. L.** (1988). The dauer larva. In *TheNematode Caenorhabditis elegans* (ed.
923 W. B. WOODC. old Spring Harbor Laboratory, Cold Spring Harbor, N. Y.), pp.
924 393–412.

925 **Robin, F. B., McFadden, W. M., Yao, B. and Munro, E. M.** (2014). Single-molecule
926 analysis of cell surface dynamics in Caenorhabditis elegans embryos. *Nat.*
927 *Methods* **11**, 677–682.

928 **Rodriguez, J., Peglion, F., Martin, J., Hubatsch, L., Reich, J., Hirani, N.,**
929 **Gubieda, A. G., Roffey, J., Fernandes, A. R., St Johnston, D., et al.** (2017).
930 aPKC Cycles between Functionally Distinct PAR Protein Assemblies to Drive
931 Cell Polarity. *Dev. Cell*.

932 **Rose, L. and Gönczy, P.** (2014). Polarity establishment, asymmetric division and
933 segregation of fate determinants in early C. elegans embryos. *WormBook* 1–43.

934 **Rual, J.-F., Ceron, J., Koreth, J., Hao, T., Nicot, A.-S., Hirozane-Kishikawa, T.,**
935 **Vandenhaute, J., Orkin, S. H., Hill, D. E., van den Heuvel, S., et al.** (2004).
936 Toward improving Caenorhabditis elegans phenome mapping with an
937 ORFeome-based RNAi library. *Genome Res.* **14**, 2162–8.

938 **Sato, K., Sato, M., Audhya, A., Oegema, K., Schweinsberg, P. and Grant, B. D.**
939 (2006). Dynamic regulation of caveolin-1 trafficking in the germ line and embryo
940 of Caenorhabditis elegans. *Mol. Biol. Cell* **17**, 3085–94.

941 **Schenk, C., Bringmann, H., Hyman, A. A. and Cowan, C. R.** (2010). Cortical
942 domain correction repositions the polarity boundary to match the cytokinesis
943 furrow in C. elegans embryos. *Development* **137**, 1743–53.

944 **Schonegg, S. and Hyman, A. A.** (2006). CDC-42 and RHO-1 coordinate acto-
945 myosin contractility and PAR protein localization during polarity establishment in
946 C. elegans embryos. *Development* **133**, 3507–16.

947 **Schonegg, S., Constantinescu, A. T., Hoege, C. and Hyman, A. A.** (2007). The
948 Rho GTPase-activating proteins RGA-3 and RGA-4 are required to set the initial
949 size of PAR domains in Caenorhabditis elegans one-cell embryos. *Proc. Natl.*
950 *Acad. Sci. U. S. A.* **104**, 14976–81.

951 **Severson, A. F. and Bowerman, B.** (2003). Myosin and the PAR proteins polarize
952   microfilament-dependent forces that shape and position mitotic spindles in
953   Caenorhabditis elegans. *J. Cell Biol.* **161**,.

954 **Shelton, C. A. and Bowerman, B.** (1996). Time-dependent responses to glp-1-
955   mediated inductions in early C. elegans embryos. *Development* **122**, 2043–50.

956 **Shelton, C. A., Carter, J. C., Ellis, G. C. and Bowerman, B.** (1999). The
957   Nonmuscle Myosin Regulatory Light Chain Gene mlc-4 Is Required for
958   Cytokinesis, Anterior-Posterior Polarity, and Body Morphology during
959   Caenorhabditis elegans Embryogenesis. *J. Cell Biol.* **146**,.

960 **Thielicke, W. and Stamhuis, E. J.** (2014). PIVlab – Towards User-friendly,
961   Affordable and Accurate Digital Particle Image Velocimetry in MATLAB. *J. Open*
962   *Res. Softw.* **2**,.

963 **Tse, Y. C., Werner, M., Longhini, K. M., Labbe, J.-C., Goldstein, B. and Glotzer,**
964   **M.** (2012). RhoA activation during polarization and cytokinesis of the early
965   Caenorhabditis elegans embryo is differentially dependent on NOP-1 and CYK-
966   4. *Mol. Biol. Cell* **23**, 4020–31.

967 **Várnai, P. and Balla, T.** (1998). Visualization of Phosphoinositides That Bind
968   Pleckstrin Homology Domains: Calcium- and Agonist-induced Dynamic Changes
969   and Relationship to Myo-[3H]inositol-labeled Phosphoinositide Pools. *J. Cell*
970   *Biol.* **143**,.

971 **Wang, S.-C., Low, T. Y. F., Nishimura, Y., Gole, L., Yu, W. and Motegi, F.** (2017).
972   Cortical forces and CDC-42 control clustering of PAR proteins for
973   Caenorhabditis elegans embryonic polarization. *Nat. Cell Biol.* **19**, 988–995.

974 **Weinkove, D., Bastiani, M., Chessa, T. A. M., Joshi, D., Hauth, L., Cooke, F. T.,**
975   **Divecha, N. and Schuske, K.** (2008). Overexpression of PPK-1, the
976   Caenorhabditis elegans Type I PIP kinase, inhibits growth cone collapse in the
977   developing nervous system and causes axonal degeneration in adults. *Dev. Biol.*
978   **313**, 384–397.

979 **Wilson, C. A., Tsuchida, M. A., Allen, G. M., Barnhart, E. L., Applegate, K. T.,**
980   **Yam, P. T., Ji, L., Keren, K., Danuser, G. and Theriot, J. A.** (2010). Myosin II
981   contributes to cell-scale actin network treadmilling through network disassembly.

982   *Nature* **465**, 373–7.

983   **Wu, C.-Y., Lin, M.-W., Wu, D.-C., Huang, Y.-B., Huang, H.-T. and Chen, C.-L.**
984   (2014). The role of phosphoinositide-regulated actin reorganization in
985   chemotaxis and cell migration. *Br. J. Pharmacol.* **171**, 5541–54.

986   **Xu, X., Guo, H., Wycuff, D. L. and Lee, M.** (2007). Role of phosphatidylinositol-4-
987   phosphate 5' kinase (ppk-1) in ovulation of Caenorhabditis elegans. *Exp. Cell*
988   *Res.* **313**, 2465–75.

989   **Yin, H. L. and Janmey, P. A.** (2003). Phosphoinositide Regulation of the Actin
990   Cytoskeleton. *Annu. Rev. Physiol.* **65**, 761–789.

991   **Zhang, L., Mao, Y. S., Janmey, P. A. and Yin, H. L.** (2012). Phosphatidylinositol 4,
992   5 Bisphosphate and the Actin Cytoskeleton.pp. 177–215. Springer, Dordrecht.

993

994

Figure legends

Fig. 1. The PIP$_2$ biomarker GFP::PH$^{PLC1\delta1}$ is enriched in dynamic cortical structures

(A-J) Differential interference contrast (DIC) (A, C, E, G, I, middle plane of the embryo) and spinning disk confocal imaging (B, D, F, H, J, cortical plane of a different embryo at the corresponding stages, with boxed regions magnified below) of one-cell *C. elegans* embryos at the indicated stages expressing GFP::PH$^{PLC1\delta1}$ monitoring PIP$_2$. Unless indicated otherwise, scale bar in this and subsequent figures: 10 µm. Time is indicated in minutes:seconds, with 00:00 corresponding to the time of centration/rotation (t_0 in K-M). See also Movie 1. Here and in all subsequent figures, the embryo anterior is to the left.

(K) Fraction of cell cortex covered by PIP$_2$ structures. The timing of pseudocleavage and mitosis are indicated. Here and in similar subsequent panels: anterior (orange) and posterior (green) quantitative data is shown, with the mean and the standard deviation. N=39 embryos for K-M.

(L) Average cortical area covered by PIP$_2$ structures over time.

(M) Elongation Index of PIP$_2$ cortical structures over time. Larger values correspond to most elongated shapes.

Fig. 2. PIP$_2$ cortical structures depend on A-P polarity

(A, B) Dual color spinning disk confocal cortical imaging of *C. elegans* embryos at the pseudocleavage stage harboring the indicated pairs of fusion proteins; the column on the right shows high magnification views of the boxed regions. (A) mCherry::PH$^{PLC1\delta1}$ and GFP::PAR-2, N=5. (B) mCherry::PH$^{PLC1\delta1}$ and GFP::PAR-6, N=5; note that elongated cortical structures (arrowhead) but not foci (arrow) of GFP::PAR-6 overlap with mCherry::PH$^{PLC1\delta1}$ cortical structures. See also Movie 2.

(C, E, G) Cortical plane images at pseudocleavage from movies acquired by spinning disk confocal imaging of control (C), *par-3*(*RNAi*) (E, N=10) or *par-2*(*RNAi*) (G, N=11) *C. elegans* embryos expressing GFP::PH$^{PLC1\delta1}$.

(D, F, H) Fraction of cell cortex covered by PIP$_2$ structures on the anterior (orange) and posterior (green) side in the conditions corresponding to (C, E, G).

36

1028 **Fig. 3. PIP$_2$ cortical structures overlap with ECT-2, CDC-42, RHO-1, and partially**

1029 **with actin**

1030 **(A-E)** Dual color spinning disk confocal cortical imaging of *C. elegans* embryos at the

1031 pseudocleavage stage harboring the indicated pairs of fusion proteins; the column on

1032 the right shows high magnification views of the boxed regions. (A)

1033 mNeonGreen::PH$^{PLC1\delta1}$ and Lifeact::mKate-2, N=46; See also Movie 3. (B)

1034 mCherry::PH$^{PLC1\delta1}$ and GFP::NMY-2, N=9; See also Movie 4. (C) mCherry::PH$^{PLC1\delta1}$

1035 and GFP::RHO-1, N=9; (D) mCherry::PH$^{PLC1\delta1}$ and GFP::CDC-42, N=7; See also

1036 Movie 5. (E) mKate2-PH$^{PLC1\delta1}$ and GFP::ECT-2, N=13.

1037

1038 **Fig. 4. Coupling between PIP$_2$ cortical structures and F-actin**

1039 **(A)** First column: representative fluorescent images of spinning disk confocal cortical

1040 imaging of embryos expressing mNG::PH$^{PLC1\delta1}$ and Lifeact::mKate-2 used to perform

1041 the PIV analysis. Second column: binary images of thresholded fluorescent images.

1042 Third column: PIV velocity vectors (high magnification views of the boxed regions on

1043 the right), arrow direction and length represent flow direction and velocity,

1044 respectively.

1045 **(B)** mNG::PH$^{PLC1\delta1}$ flow velocity plotted as a function of Lifeact::mKate-2 velocity in

1046 the same position and at the same time. Data points are represented with a color

1047 scale dependent on their spatial density, from denser to sparser (red, yellow, light

1048 blue). Pearson correlation coefficient: $\rho=0.61$, $p=0$ with Matlab precision, Student's t

1049 test. N=13 embryos for B-D.

1050 **(C)** Angle distribution between flow velocity vectors of mNG::PH$^{PLC1\delta1}$ and

1051 Lifeact::mKate-2 in the same position and at the same time. The angle distribution

1052 peaks at $\theta = 0°$ and decays exponentially thereafter (cutoff angle: $\theta=38°$). Two

1053 independent velocity fields cannot result in the observed angle distribution

1054 (probability: $p=0$ with Matlab precision (shi2-test)).

1055 **(D)** Cross-correlation between thresholded binary movies of mNG::PH$^{PLC1\delta1}$ and

1056 Lifeact::mKate-2; Lifeact::mKate-2 was shifted with different time intervals relative to

1057 mNG::PH$^{PLC1\delta1}$. The boxed region is magnified on the right, showing that average

1058 maximal overlap is achieved with a time shift of $\Delta t = $ -9.3 +/- 1.5 seconds (average

1059 and standard deviation), irrespective of the order in which the two signals were

1060 recorded (Materials and Methods). See also Movie 6.

1061 **(E)** Embryo expressing mNG::PH$^{PLC1\delta1}$ and Lifeact::mKate-2 imaged every 4.2

1062 seconds; the boxed region is magnified on the right and shows snapshots from

1063 corresponding movie illustrating that mNeonGreen::PH$^{PLC1\delta1}$ (white arrow) moves

1064 ahead of Lifeact::mKate-2.

1065 **(F, H, J)** Cortical plane images at pseudocleavage from spinning disk confocal

1066 imaging of *C. elegans* embryos treated as indicated and expressing GFP::PH$^{PLC1\delta1}$.

1067 (F) *nmy-2*(*RNAi*), N=7; (H) *act-1*(*RNAi*), N=8 at pseudocleavage and N=12 at mitosis;

1068 (J) *tba-2*(*RNAi*), N=10. Note that both *act-1*(*RNAi)* and *tba-2*(*RNAi*) correspond to

1069 severe but partial depletion conditions, as more complete depletion results in sterility.

1070 Arrowhead: remaining PIP$_2$ structure.

1071 **(G, I, K)** Fraction of cell cortex covered by PIP$_2$ structures on the anterior (orange)

1072 and posterior (green) of *nmy-2*(*RNAi*) (G, N=7), *act-1*(*RNAi*) (I, N= 8 at

1073 pseudocleavage, N=12 at mitosis) or *tba-2*(*RNAi*) (K, N=10) embryos.

1074

1075 **Fig. 5. Proper PIP$_2$ cellular level is essential for correct organization of the actin**

1076 **cytoskeleton**

1077 **(A-I)** Confocal spinning disk imaging of embryos expressing GFP::PH$^{PLC1\delta1}$ and

1078 Lifeact::mKate-2 (A-C: middle plane, D-I: cortical plane).

1079 **(A)** DMSO treated *perm-1*(*RNAi*) control embryos.

1080 **(B, C)** *perm-1*(*RNAi*) embryos treated with Ionomycin/Ca^{2+}. $t_{1/2}$=00:00: time at which

1081 half of plasma membrane GFP::PH$^{PLC1\delta1}$ fluorescence disappeared; the time stamps

1082 are shown in yellow here and in following figure panels where $t_{1/2}$=00:00. N=17, all

1083 stages combined. (B) $t_{1/2}$ at pseudocleavage. Note that the absence of coverslip,

1084 which is needed to preserve fragile *perm-1*(*RNAi*) embryos, prevents their flattening,

1085 such that they are more contractile. Note also that the pseudocleavage furrow moves

1086 towards the anterior and either remains there until the end of the first cell cycle (N=4,

1087 as shown) or relaxes (N=4, not shown) (C) $t_{1/2}$ at mitosis. Note that whereas embryos

1088 were dissected in the drug-containing solution, drug action (as monitored by $t_{1/2}$) took

1089 place > 6 min after polarity was established. See also Movie 7.

1090 **(D-I)** Control (D, G) and *ocrl-1*(*RNAi*) *unc-26*(*s1710*) (E, F, H, I) embryo during

1091 pseudocleavage (D, E, F) or mitosis (G, H, I). (E, H) class 1 phenotype (GFP::PH

1092 $^{PLC1\delta1}$: N=27/48, Lifeact::mKate-2: N=4/11); arrow: immotile structure, arrowhead:

1093 motile structure. (F, I) class 2 phenotype (GFP::PH$^{PLC1\delta1}$: N=21/48, Lifeact::mKate-2:

38

1094   N=7/11). White dashed line in (G-I) show the position utilized to create the

1095   corresponding kymographs in (J-L). See also Movie 9.

1096   **(J-L)** Kymographs corresponding to the above movies aligned at cytokinesis arrow:

1097   immotile structure, arrowhead: motile structure; Note that motile cortical PIP$_2$

1098   structures eventually move towards the cleavage furrow, which partly corrects the

1099   aberrant PIP$_2$ cortical domain distribution, consistent with the presence of a

1100   mechanism correcting mispositioned cortical domains operating at this stage (Schenk

1101   et al., 2010). Entire durations of the kymographs, in min:sec: (J) 16:30, (K) 20:00, (L)

1102   19:00.

1103

1104

1105   **Fig. 6. Proper PIP$_2$ cellular level is essential for correct PAR polarity**

1106   **(A-C, G-I)** Confocal spinning disk cortical imaging of control (A, G) or *ocrl-1*(*RNAi*)

1107   *unc-26*(*s1710*) (B, C, H, I) embryos expressing mCherry::PH$^{PLC1\delta1}$ and GFP::PAR-6

1108   (A-C, N=5/9 class I, N=4/9 class II) or GFP::PAR-2 (G-I, N=12/22 class I; N=10/22

1109   class II). White dashed lines indicate positions used to create the corresponding

1110   kymographs in. See also Movies 10, 11.

1111   **(D-F,J-L)** Kymographs corresponding to the above movies aligned at cytokinesis.

1112   Entire durations of the kymographs, in min:sec: (D) 16:40, (E) 11:20, (F) 17:40, (G)

1113   17:40, (H) 17:40, (I) 17:40.

1114   **(M-O)** Images acquired by confocal imaging of embryos expressing GFP::PAR-2, 4.5

1115   μm below the cortical plane. The dashed line marks the boundary of the PAR-2

1116   domain. (M): DMSO treated control *perm-1*(*RNAi*) embryo. (N, O): *perm-1*(*RNAi*)

1117   embryo treated with Ionomycin/Ca^{2+} (t$_{1/2}$=00:00) during pseudocleavage, N=6; during

1118   mitosis, N=3).Note: worms were dissected in the drug, but drug action (t$_{1/2}$) took place

1119   > 6 min after polarity was established**.** See Movies 12, 13, 14.

1120

1121   **Fig. 7. F-actin impairment affects GFP::PAR-2 also during polarity maintenance**

1122   **(A-C)** Confocal spinning disk cortical imaging of *perm-1*(*RNAi*) embryos expressing

1123   GFP::PAR-2 and Lifeact::mKate-2 (middle plane), treated during early

1124   centration/rotation either with DMSO (A, N=6), Cytochalasin D (B, N=5, note that this

1125   movie was acquired with bining=2), or Latrunculin A (C, N=18). Arrowhead points to

1126   plasma membrane invagination (Redemann et al., 2010). See Movies 15, 16.

1127   **(D)** Graphical summary and working model (not to scale). PIP_2 is enriched in dynamic

1128   and polarized structures at the cortex of one-cell *C. elegans* embryos. These

1129   structures move ahead of F-actin fibers, with which their velocity and direction is

1130   correlated. Moreover, the two components exhibit mutually reciprocal requirements,

1131   as the formation of PIP_2 cortical structures requires F-actin, whereas a proper PIP_2

1132   level is essential for F-actin network organization. Moreover, through its ability to

1133   properly reorganize the F-actin network, PIP_2 is essential for proper sizing of PAR

1134   domains and thus for A-P polarity establishment and maintenance. In addition, there

1135   might be an actin independent pathway through which PIP_2 regulates polarity. See

1136   text for further details. Note that in the cortical embryo schematic on the top right, for

1137   simplicity only those F-actin filaments that move in concert with PIP_2 cortical
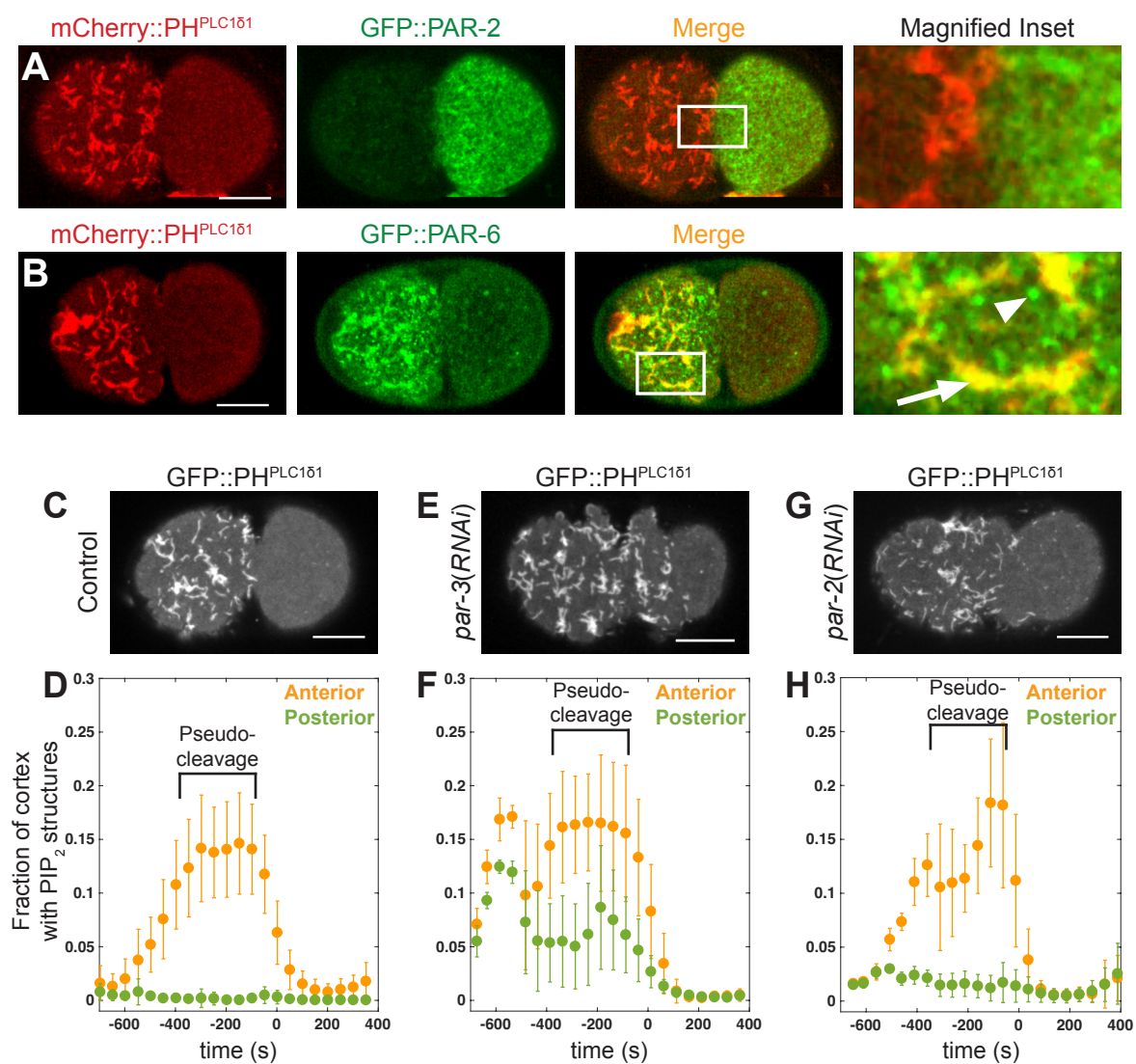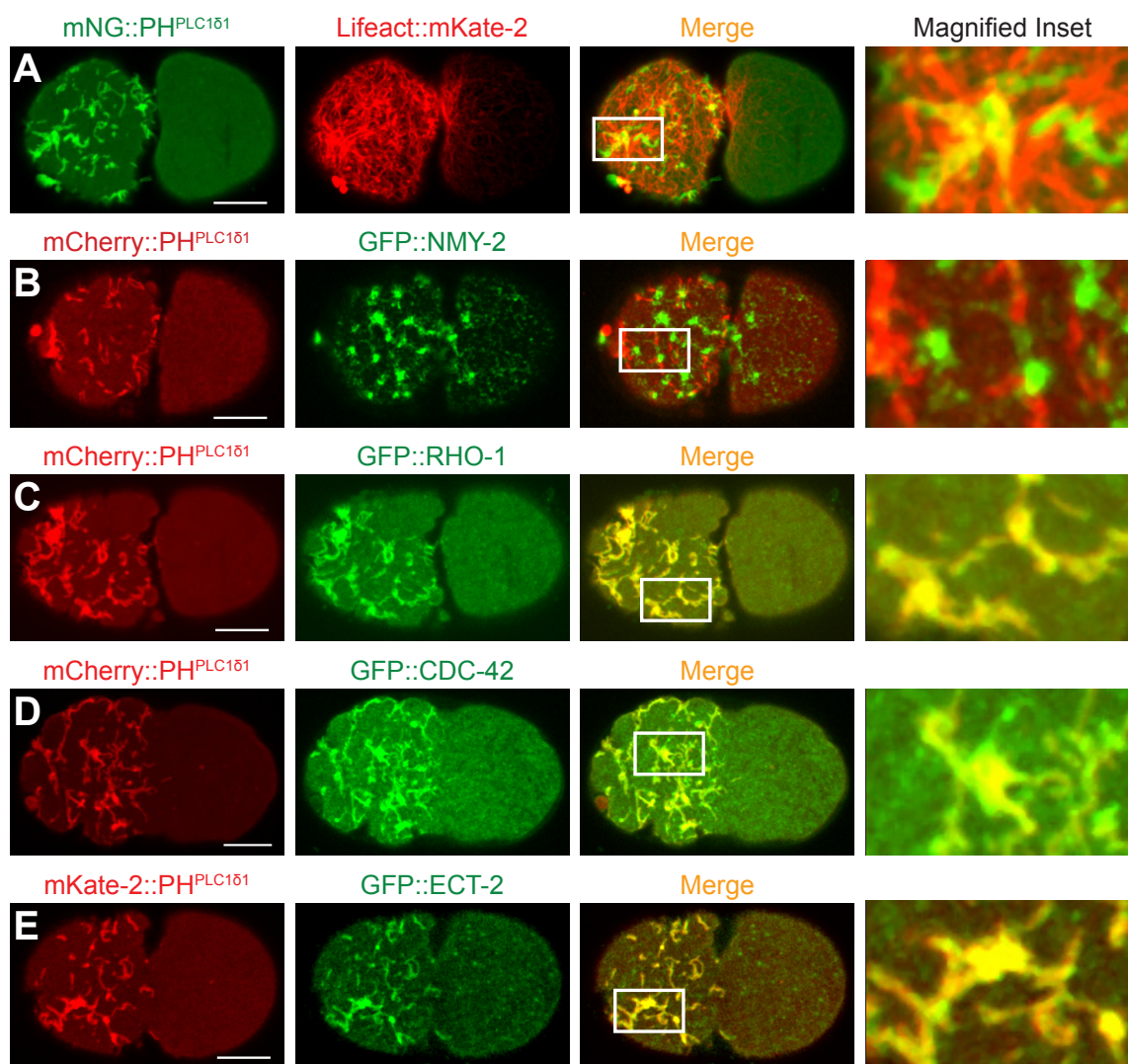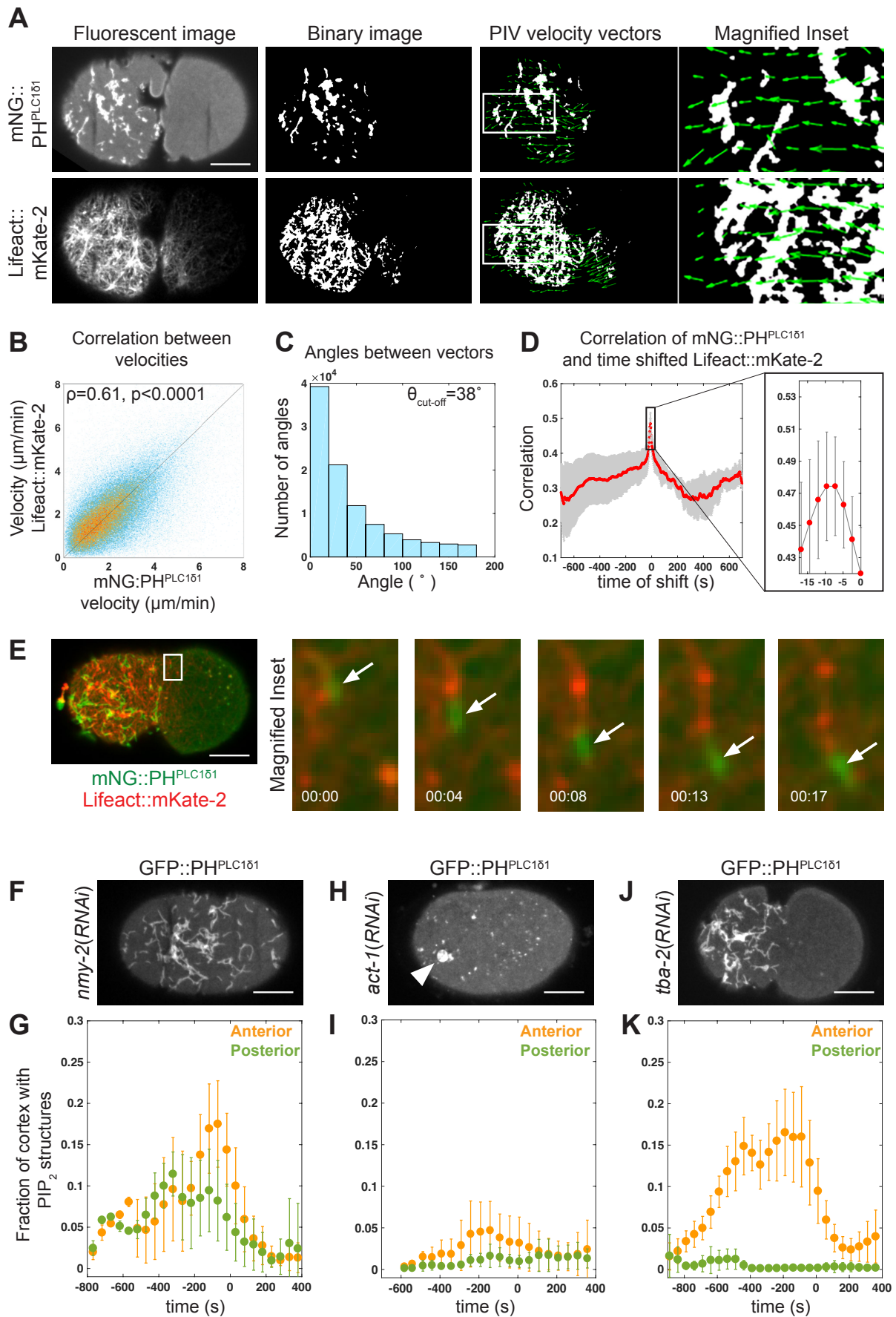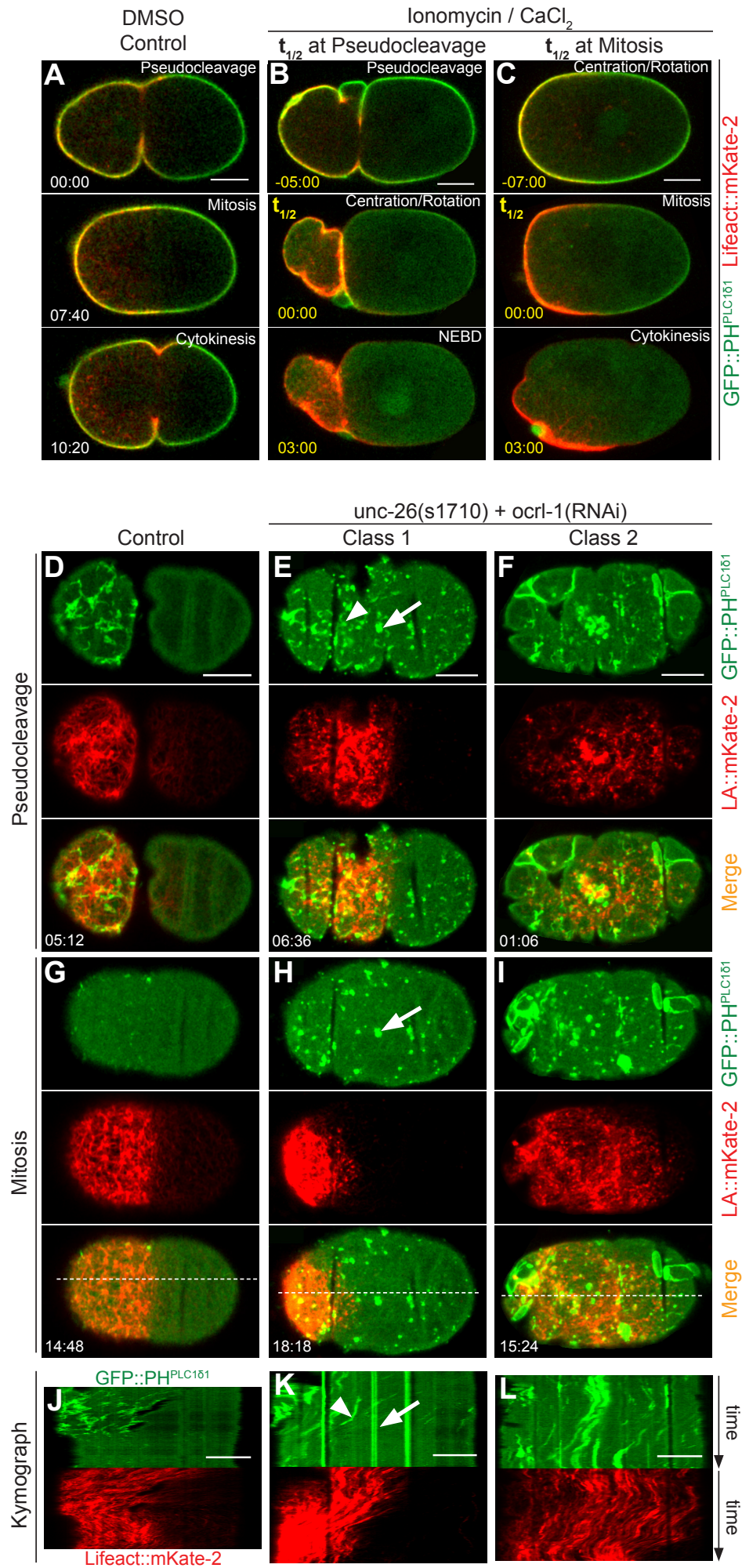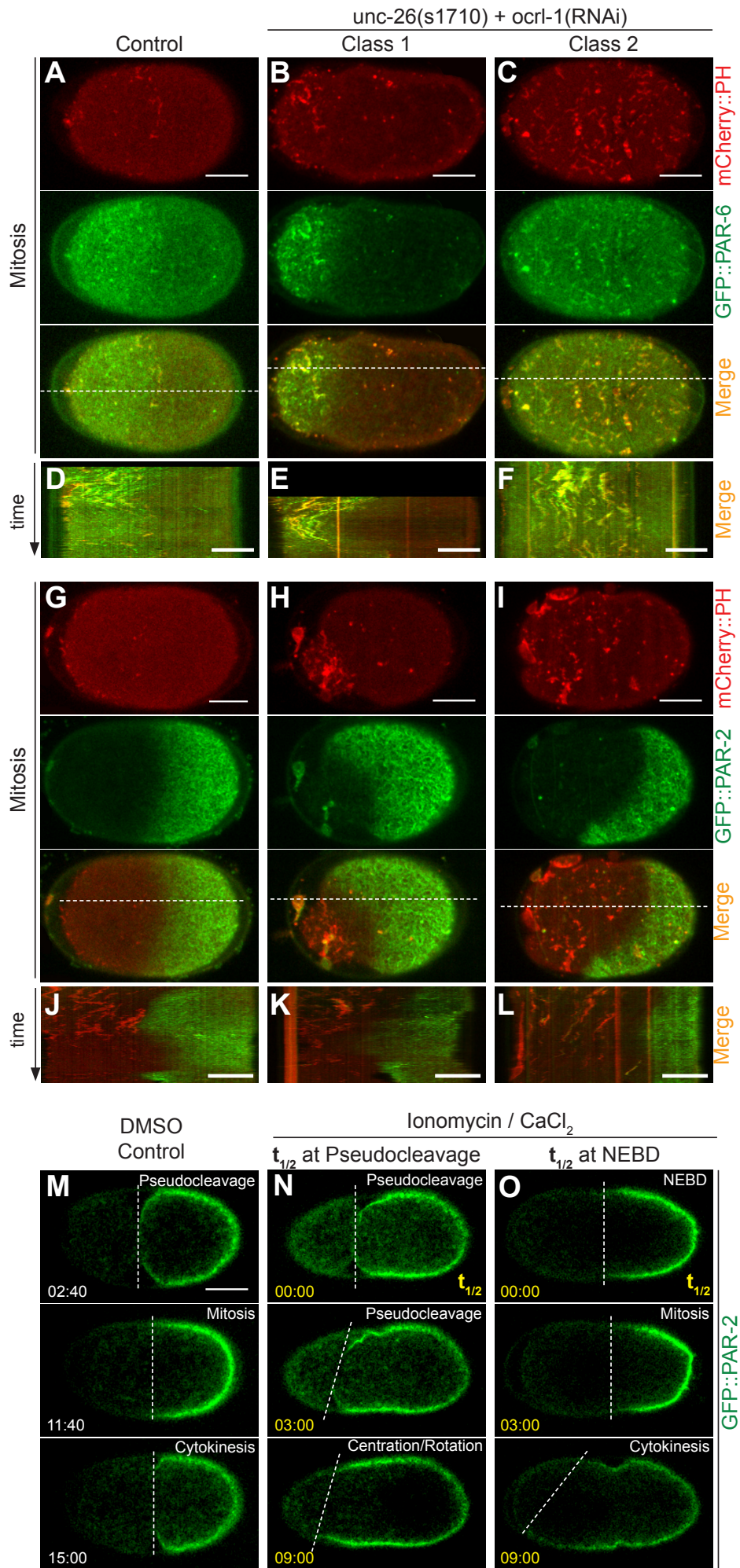
1138   structures are represented.

1139
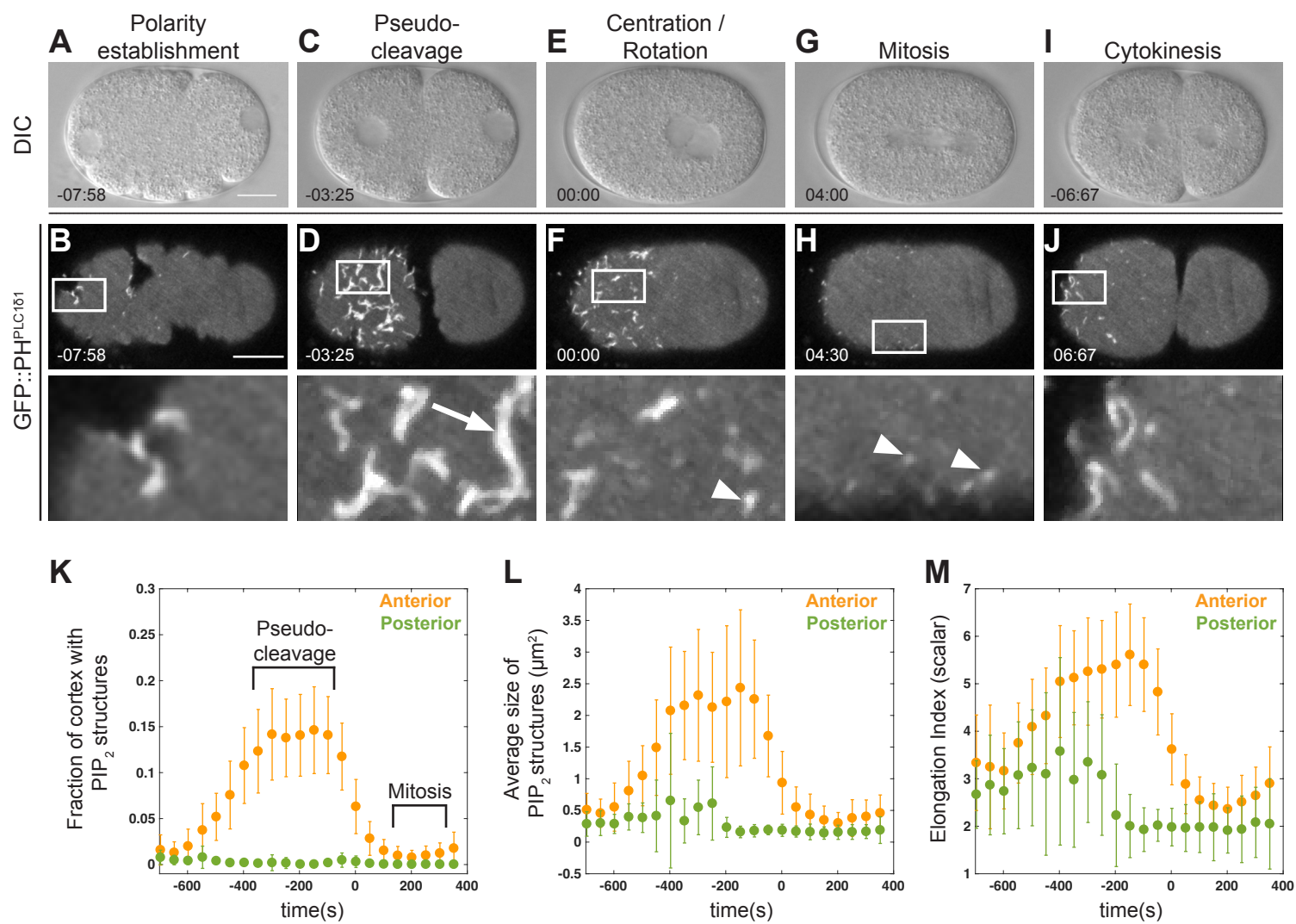
Figure 1

Figure 2

Figure 3

Figure 4

Figure 5

Figure 6

Figure 7